Open Research Online

The Open University's repository of research publications
and other research outputs

Timing and conditions of peak metamorphism and cooling across the Zimithang Thrust, Arunachal Pradesh, India

Journal Item

For guidance on citations see FAQs.

Version: Version of Record

oro.open.ac.uk

Timing and conditions of peak metamorphism and cooling across the Zimithang Thrust, Arunachal Pradesh, India

Clare J. Warren [a,*], Athokpam K. Singh [b], Nick M.W. Roberts [c], Daniele Regis [a], Alison M. Halton [a], Rajkumar B. Singh [b]

[a] *Department of Environment, Earth and Ecosystems, The Open University, Milton Keynes MK7 6AA, UK*
[b] *Petrology and Geochemistry Group, Wadia Institute of Himalayan Geology, Dehradun 248001, India*
[c] *NERC Isotope Geosciences Laboratory, British Geological Survey, Nottingham NG12 5GG, UK*

ABSTRACT

The Zimithang Thrust juxtaposes two lithotectonic units of the Greater Himalayan Sequence in Arunachal Pradesh, NE India. Monazite U–Pb, muscovite $^{40}Ar/^{39}Ar$ and thermobarometric data from rocks in the hanging and footwall constrain the timing and conditions of their juxtaposition across the structure, and their subsequent cooling. Monazite grains in biotite–sillimanite gneiss in the hanging wall yield LA-ICP-MS U–Pb ages of 16 ± 0.2 to 12.7 ± 0.4 Ma. A schistose gneiss within the high strain zone yields overlapping-to-younger monazite ages of 14.9 ± 0.3 to 11.5 ± 0.3 Ma. Garnet–staurolite–mica schists in the immediate footwall yield monazite ages of 27.3 ± 0.6 to 17.1 ± 0.2 Ma. Temperature estimates from Ti-in-biotite and garnet–biotite thermometry suggest similar peak temperatures were achieved in the hanging and footwalls (~525–650 °C). Elevated temperatures of ~700 °C appear to have been reached in the high strain zone itself and in the footwall further from the thrust. Single grain fusion $^{40}Ar/^{39}Ar$ muscovite data from samples either side of the thrust yield ages of ~7 Ma, suggesting that movement along the thrust juxtaposed the two units by the time the closure temperature of Ar diffusion in muscovite had been reached. These data confirm previous suggestions that major orogen-parallel out-of-sequence structures disrupt the Greater Himalayan Sequence at different times during Himalayan evolution, and highlight an eastwards-younging trend in $^{40}Ar/^{39}Ar$ muscovite cooling ages at equivalent structural levels along Himalayan strike.

1. Introduction

Differences in the pressure–temperature–time (PTt) evolution of metamorphic rocks across lithologies and tectonic structures yield information about the rates and timescales of processes that act to transform rocks in plate collision zones. The archetypal modern orogen formed by continent-continent collision, the Himalaya, provides excellent material for investigating how, when, and how fast, rocks are transported and transformed deep within collision zones and subsequently exhumed back to the surface.

The Himalaya are the surface expression of the India–Asia collision, which initiated 55–50 million years ago (Rowley, 1996, 1998; Zhu et al., 2005). During collision, material that originally formed the Indian continental margin was buried beneath the Asian continent, metamorphosed, and subsequently exhumed along the orogenic front. Despite numerous conceptual models for how the Himalaya formed

(e.g. Beaumont et al., 2001; Burchfiel et al., 1992), there remains debate about the mechanism(s) driving the exhumation of the Himalayan high-grade metamorphic core of the Himalaya and how these mechanisms may have changed over time.

The high-grade rocks that comprise the core of the Himalayan orogen form what is known as the Greater Himalayan Sequence (e.g. GHS; Hodges, 2000 and references therein). This unit is separated from the overlying Tethyan Sedimentary Sequence (TSS) by the low-angle brittle–ductile normal-sense South Tibetan Detachment (STD) and from the underlying Lesser Himalayan Sequence (LHS) by the low-angle brittle–ductile Main Central Thrust (MCT). The GHS comprises amphibolite to granulite facies metapelites, meta-granitoids and subordinate metabasites. The metapelites are variably migmatized and transected by Oligocene to Miocene-aged leucogranite veins, dykes, sheets and plutons of varying dimensions, most of which were formed by partial melting of metapelites, similar in composition to those into which they intrude (e.g. Hodges, 2000 and references therein).

The PTt history of different structural levels of the GHS, as well as the history of equivalent structural levels at different places along orogenic

* Corresponding author.
  E-mail address: clare.warren@open.ac.uk (C.J. Warren).

strike, provides insight into the burial and exhumation history as well as the tectonic processes driving crustal deformation. There appears to be significant heterogeneity in the along-strike timing of the high-temperature history of the upper structural levels of the GHS from the central to the eastern parts of the orogen. The structurally-highest amphibolite and granulite-grade metapelites in Nepal reached their peak conditions at 38–30 Ma (Corrie and Kohn, 2011; Simpson et al., 2000), whereas those in Sikkim are dated at 28–23 Ma (Rubatto et al., 2013), and those in NW Bhutan are dated at 15–13 Ma (Warren et al., 2011a; Grujic et al., 2011). Moreover, $^{40}Ar/^{39}Ar$ muscovite and/or biotite ages from similar samples also young eastwards, with ~15 Ma ages reported from the Everest region of Nepal (Carosi et al., 1998), ~13 Ma ages from Sikkim (Kellett et al., 2013), ~11 Ma ages from central Bhutan (Maluski et al., 1988) and ~7–12 Ma ages in NW Arunachal Pradesh (Yin et al., 2010).

Breaks or abrupt changes in PTt history suggest the location of 'cryptic' discontinuities in multiple places in the central and eastern Himalaya, which are not always obvious in the field, e.g. the Banuwa and Sinuwa Thrusts in central Nepal (e.g. Corrie and Kohn, 2011), the High Himal Thrust in eastern Nepal (Imayama et al., 2012), the Kakthang and/or Laya Thrust system in Bhutan (Warren et al., 2011a; Chakungal et al., 2010; Gansser, 1983) and the Zimithang Thrust in Arunachal Pradesh, NE India (Yin et al., 2006, 2010). The significance of these discontinuities or faults in terms of orogenic driving forces and deformation mechanisms remains unclear, partly because the timing of their motion remains somewhat unconstrained.

In central to eastern Nepal, the timing of attainment of peak metamorphic temperatures and associated melting generally gets older toward structurally higher levels (Corrie and Kohn, 2011; Imayama et al., 2012). The PTt data, and the discontinuities between different sections, have been interpreted as a result of progressive stacking of thrust slices along the Sinuwa, Banuwa and Main Central Thrusts as the GHS exhumed. In NW Bhutan, however, some of the youngest rocks and highest-grade rocks are found at the structurally highest levels of the GHS (Warren et al., 2011a; Grujic et al., 2011), separated from younger, lower-grade metamorphic rocks by the cryptic out-of-sequence Laya Thrust.

The aim of this study was to constrain the timing of motion of the previously reported Zimithang Thrust, the purported eastwards extension of the Kakthang Thrust in Arunachal Pradesh, east of Bhutan (e.g., Yin et al., 2006, 2010) and the timing of metamorphism and cooling in the lithotectonic units it juxtaposed. U–Pb monazite and $^{40}Ar/^{39}Ar$ muscovite and biotite ages are documented from hanging and footwall rocks, and the data are compared with along-strike trends in ages of high temperature metamorphism, melting and cooling further westwards toward Central Nepal. The data show that monazite crystallized later in the hanging wall (~17–11.5 Ma) than in the footwall (~27–17 Ma), but that both units cooled together through the closure temperature for Ar diffusion in muscovite by ~7 Ma. The data furthermore suggest that peak metamorphic grade was reached at a similar time in the hanging walls of the Laya (Bhutan) and Zimithang (Arunachal) Thrusts but that the rocks cooled more slowly (thus yielding younger $^{40}Ar/^{39}Ar$ ages) in Arunachal.

2. Geological setting

The higher structural levels of the GHS in Arunachal are mainly comprised of high-grade sillimanite-bearing migmatitic gneisses, equivalent to those described from similar structural levels along orogenic strike (e.g. Gansser, 1983; Hodges, 2000). Poor access and limited exposure has hampered detailed mapping and structural understanding. Toward Tawang (Fig. 1), the migmatitic gneisses are overlain by kyanite schists, which grade upwards into staurolite-garnet and garnet-only schists. Around the town of Lumla, an apparently thrust-bound window exposing 'Lumla Formation (LF)' metasediments has been described (e.g. Yin et al., 2010). These metasedimentary rocks mainly comprise quartzites,

micaceous quartzites and phyllites, that grade upwards into garnet-bearing lithologies near the contacts with the overlying the higher-grade metasedimentary rocks. The LF has been interpreted as a structurally lower unit (potentially with LHS affinity) exposed as a window through the GHS (Yin et al., 2006, 2010; Fig. 1). The contact between the LF and the overlying higher-grade rocks has been described as a 0.3–0.5 m thick gouge zone (Yin et al., 2006, 2010) and therefore considered to be tectonic rather than depositional. This 'Lumla Thrust' cuts parallel to the foliation and may be a northerly exposure through the MCT, similar to the structure separating the Paro window from the GHS in southwestern Bhutan (e.g. Gansser, 1983; Tobgay et al., 2010).

To the north of Lumla, high-grade garnet-bearing mica schists and gneisses are over-thrust by garnet-free sillimanite-bearing augen gneisses along the 'Zimithang Thrust', a possible out-of-sequence structure correlated with the Kakhtang thrust in Bhutan (Grujic et al., 1996; Yin et al., 2006, 2010; Fig. 1). Field observations of this structure are detailed in Yin et al., 2010: mylonitic augen gneiss is juxtaposed against garnet–biotite gneiss across a to-the-south-sense shear structure. Four gneisses sampled from the hanging wall of the ZT (RAK 21A, 23, 25, 28), one from the ZT shear zone itself (RAK 29), five samples from the footwall (RAK 30, 31A, 433, 439 and 421), and two samples from the Lumla Formation (RAK 33A and 36) were analyzed for thermobarometric constraints and U–Pb and $^{40}Ar/^{39}Ar$ geochronology (Fig. 1).

3. Sample petrography and mineral chemistry

Major-element compositions of the rock-forming minerals were analyzed using the Open University Cameca SX-100 5 wavelength-dispersive spectrometer electron microprobe using a defocused beam with spot size of 10 μm, and conditions of 15 kV, 20 nA and 30s collection time. Calibrations were performed on natural standards and analyses were corrected using a ZAF matrix correction routine. Analyses were bracketed by analyses of secondary standards to check for major element reproducibility of 1%. Average mineral chemistry data are presented in Table 1. Where mineral chemistry differs with microstructural position, or due to zoning, the different compositions are noted. Thin-section photomicrographs of all samples are shown in Fig. 2. Oriented samples were not available for analysis. Samples are described as exposed from north to south between Zimithang and Lumla, then eastwards towards Tawang and north again to Tsokyo (Fig. 1).

RAK 21A is a weakly foliated gneiss from the hanging wall of the ZT, containing major quartz, biotite, K-feldspar and plagioclase, minor muscovite, and accessory zircon, monazite, apatite and opaques. Biotite forms elongate laths which define the weak foliation; subordinate muscovite forms crystals that generally cross-cut the main fabric.

K-feldspar varies from Or_{87-94}, with compositions appearing to vary more between grains than within grains. Plagioclase yields a more consistent composition of Ab_{84}. Biotite in all structural associations has a composition of X_{Fe} (Fe/Fe + Mg) = 0.61, and shows no compositional zoning. Muscovite is also unzoned, with 6.3 Si per 22O.

Monazite is rare, but where found, form crystals up to 200 μm in length. They are found included in biotite and as clumps of crystals associated with apatite and zircon in quartz. Th zoning is patchy and discontinuous; Y zoning is less pronounced (Fig. A1).

RAK 23 is a relatively granoblastic gneiss from the hanging wall of the ZT, containing major quartz, plagioclase, muscovite and biotite, minor garnet, and accessory opaques, apatite, zircon and monazite. Muscovite forms mm-scale laths, associated with smaller biotite grains. Muscovite is occasionally partially replaced by biotite along rims and cleavages, and contains ~6.25 Si per 22O (Fig. 3g).

K-feldspar varies from Or_{85} in the matrix, to Or_{95} inclusions in garnet. Plagioclase varies from Ab_{86} in the matrix to Ab_{91} near garnet and Ab_{84} inclusions in garnet. Biotite in all structural associations has a composition of X_{Fe} (Fe/Fe + Mg) = 0.69 and crystals are not internally zoned.

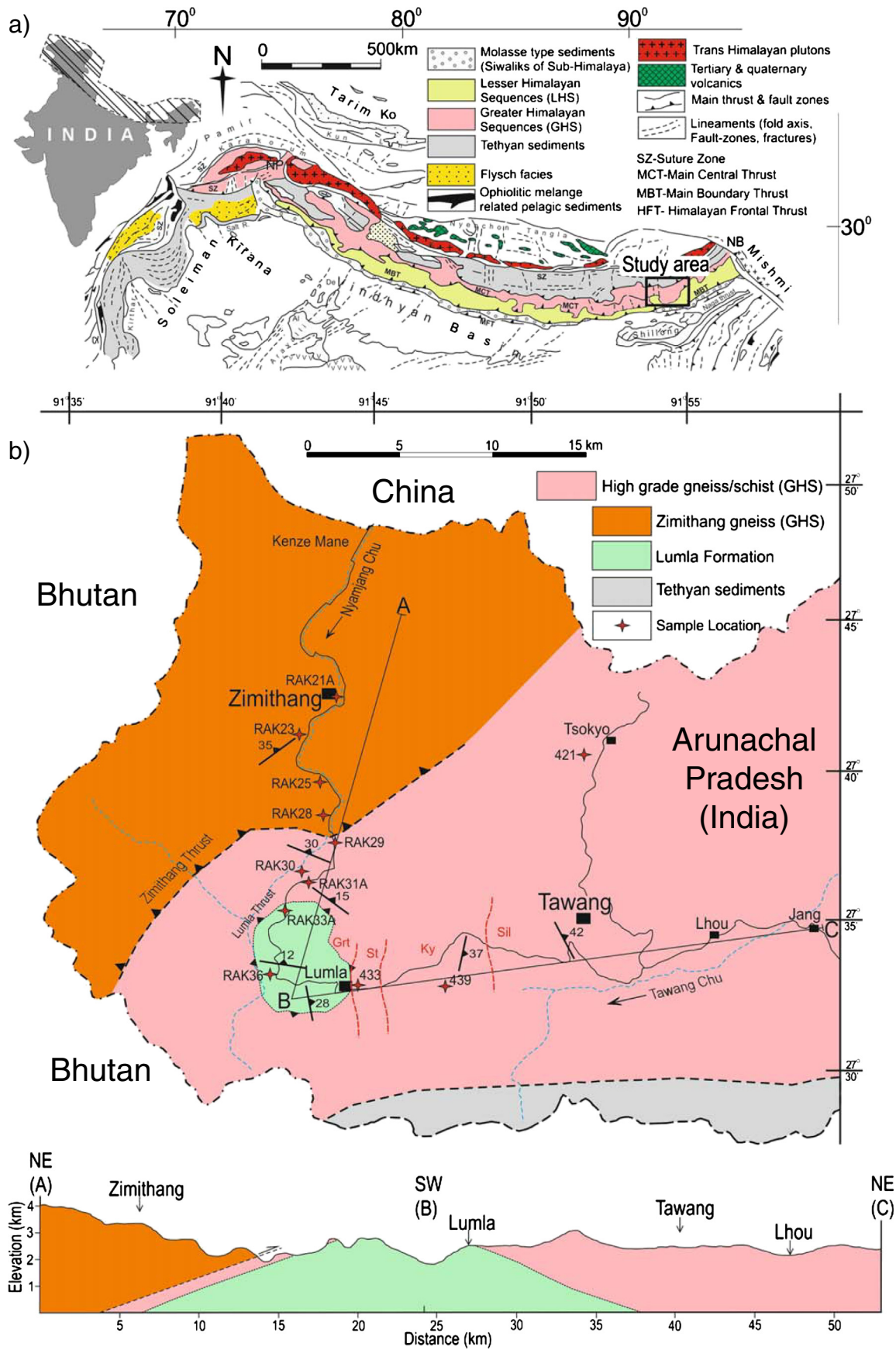**Fig. 1.** (a) Geological sketch map of the Himalayan orogen, modified after Gansser, 1974. The inset shows the extent of the Himalaya in India. (b) Geological map and cross-section across north-western Arunachal Pradesh, NE India after Yin et al., 2006 and Bikramaditya and Singh, 2014. Sample localities and metamorphic mineral isograds are marked where known. The South Tibetan Detachment does not crop out in western Arunachal Pradesh.

Table 1
Average EMP data.

Hanging wall

Sample	RAK 21A					RAK 23								
Mineral	or large	or small	ab	bt	mus	bt matrix	mus	pl matrix	pl in grt	pl nr grt	or matrix	or in grt	or nr grt	chl
n (analyses)	2	4	11	12	3	17	16	7	6	4	7	6	4	4
Na_2O	1.41	0.83	9.92	0.12	0.41	0.09	0.47	10.07	10.05	10.66	1.29	0.55	0.82	0.08
K_2O	14.60	15.42	0.27	9.53	10.91	9.23	10.79	0.25	0.24	0.23	14.83	15.46	15.45	0.01
MgO	0.00	0.00	0.00	7.61	0.89	6.03	0.72	0.00	0.00	0.00	0.00	0.00	0.00	9.57
CaO	0.04	0.02	2.96	0.01	0.01	1.07	0.05	2.83	3.10	1.60	0.04	0.03	0.02	0.27
MnO	0.00	0.01	0.01	0.16	0.00	0.24	0.01	0.00	0.08	0.01	0.00	0.03	0.02	0.39
FeO	0.01	0.01	0.02	21.30	1.44	23.73	1.75	0.03	0.53	0.06	0.01	0.21	0.18	32.82
Al_2O_3	18.54	18.26	21.67	18.19	33.13	18.60	34.66	21.97	22.17	21.22	18.93	18.39	18.55	18.43
SiO_2	64.70	64.13	64.64	35.94	46.38	34.53	47.10	66.06	64.39	67.09	65.13	65.32	65.12	25.68
TiO_2	0.00	0.01	0.01	2.39	0.25	1.72	0.36	0.01	0.01	0.02	0.01	0.00	0.01	0.03
Total	99.30	98.68	99.50	95.24	93.40	95.25	95.92	101.22	100.57	100.90	100.24	99.99	100.16	87.27
Na	0.13	0.08	0.85	0.03	0.11	0.03	0.12	0.85	0.86	0.90	0.11	0.05	0.07	0.03
K	0.86	0.92	0.02	1.87	1.90	1.84	1.82	0.01	0.01	0.01	0.87	0.91	0.91	0.00
Mg	0.00	0.00	0.00	1.74	0.18	1.40	0.14	0.00	0.00	0.00	0.00	0.00	0.00	2.60
Ca	0.00	0.00	0.14	0.00	0.00	0.22	0.01	0.13	0.15	0.07	0.00	0.00	0.00	0.05
Mn	0.00	0.00	0.00	0.02	0.00	0.03	0.00	0.00	0.00	0.00	0.00	0.00	0.00	0.06
Fe	0.00	0.00	0.00	2.74	0.16	3.10	0.19	0.00	0.02	0.00	0.00	0.01	0.01	5.01
Al	1.01	1.01	1.13	3.29	5.31	3.43	5.42	1.13	1.15	1.09	1.02	1.00	1.01	3.94
Si	2.99	3.00	2.86	5.52	6.31	5.39	6.24	2.87	2.83	2.92	2.99	3.01	3.00	4.67
Ti	0.00	0.00	0.00	0.28	0.03	0.20	0.04	0.00	0.00	0.00	0.00	0.00	0.00	0.00
Total	5.00	5.00	5.00	15.50	14.00	15.63	13.99	5.00	5.03	4.99	4.99	4.97	4.99	16.37

Sample	RAK 25				RAK 28				RAK 29			
Mineral	bt	ab	or	mus	ab	or	mus	bt	ab	mus	bt	or
n (analyses)	27	14	7	26	6	2	15	17	6	9	9	9
Na_2O	0.09	10.51	1.07	0.45	11.04	0.83	0.46	0.08	11.08	0.58	0.13	0.60
K_2O	9.50	0.29	15.39	10.72	0.22	15.59	10.63	9.44	0.24	10.48	9.45	10.39
MgO	7.10	0.00	0.00	1.17	0.00	0.00	1.09	4.85	0.00	1.36	11.31	1.37
CaO	0.02	2.01	0.02	0.01	1.35	0.01	0.01	0.01	1.28	0.00	0.01	0.01
MnO	0.37	0.01	0.00	0.02	0.00	0.01	0.02	0.26	0.01	0.01	0.08	0.01
FeO	23.30	0.01	0.01	2.91	0.02	0.03	2.70	25.96	0.02	1.37	16.80	1.34
Al_2O_3	17.28	21.27	18.56	32.42	20.67	18.47	32.70	18.44	20.69	32.23	17.69	32.45
SiO_2	34.60	66.44	65.29	47.43	65.82	63.92	46.12	34.07	66.27	46.62	37.10	47.09
TiO_2	2.18	0.01	0.00	0.45	0.00	0.00	0.25	1.57	0.01	1.25	2.91	1.29
Total	94.44	100.54	100.35	95.58	99.12	98.86	93.98	94.67	99.59	93.91	95.48	94.54
Na	0.03	0.89	0.10	0.12	0.95	0.08	0.12	0.03	0.95	0.15	0.04	0.06
K	1.91	0.02	0.90	1.83	0.01	0.93	1.85	1.91	0.01	1.81	1.81	0.65
Mg	1.67	0.00	0.00	0.23	0.00	0.00	0.22	1.15	0.00	0.27	2.52	0.10
Ca	0.00	0.09	0.00	0.00	0.06	0.00	0.00	0.00	0.06	0.00	0.00	0.00
Mn	0.05	0.00	0.00	0.00	0.00	0.00	0.00	0.03	0.00	0.00	0.01	0.00
Fe	3.07	0.00	0.00	0.33	0.00	0.00	0.31	3.45	0.00	0.16	2.10	0.05
Al	3.21	1.10	1.00	5.12	1.08	1.02	5.25	3.45	1.08	5.14	3.12	1.87
Si	5.45	2.90	3.00	6.35	2.92	2.99	6.28	5.42	2.92	6.31	5.55	2.30
Ti	0.26	0.00	0.00	0.04	0.00	0.00	0.03	0.19	0.00	0.13	0.33	0.05
Total	15.65	5.00	5.00	14.02	5.02	5.01	14.06	15.64	5.02	13.97	15.48	5.07

Footwall

Sample	RAK 30								
Mineral	gt rim	gt mantle	gt core	mus	st	bt	ab in grt	ab matrix	chl
n (analyses)	1	1	1	18	12	14	10	7	3
Na_2O	0.02	0.01	0.02	1.59	0.05	0.36	8.76	10.27	0.01
K_2O	0.03	0.00	0.00	8.84	0.00	8.39	0.14	0.16	0.01
MgO	3.18	1.68	1.22	0.73	1.50	9.40	0.00	0.00	14.03
CaO	2.63	4.38	5.31	0.01	0.00	0.01	5.36	2.44	0.00
MnO	0.24	2.11	3.59	0.00	0.05	0.02	0.02	0.00	0.03
FeO	35.42	34.60	32.84	1.17	12.90	19.81	0.44	0.00	26.22
Al_2O_3	20.28	20.55	20.24	34.85	53.30	19.41	23.90	21.35	22.64
SiO_2	36.07	36.92	37.08	46.37	27.27	35.59	62.12	64.57	24.60
TiO_2	1.58	0.01	0.09	0.65	0.65	1.43	0.10	0.00	0.15
Total	99.45	100.25	100.39	94.22	95.72	94.41	100.84	98.79	87.70
Na	0.00	0.00	0.00	0.41	0.01	0.10	0.75	0.89	0.00
K	0.00	0.00	0.00	1.51	0.00	1.64	0.01	0.01	0.00
Mg	0.38	0.20	0.15	0.15	0.34	2.14	0.00	0.00	3.48
Ca	0.23	0.38	0.46	0.00	0.00	0.00	0.25	0.12	0.00
Mn	0.02	0.14	0.25	0.00	0.01	0.00	0.00	0.00	0.01
Fe	2.41	2.34	2.23	0.13	1.58	2.53	0.02	0.00	3.65
Al	1.94	1.96	1.93	5.49	9.28	3.50	1.24	1.12	4.44
Si	2.93	2.99	3.00	6.20	4.02	5.44	2.74	2.88	4.09
Ti	0.10	0.00	0.01	0.07	0.05	0.17	0.10	0.00	0.02
Total	8.01	8.03	8.03	13.95	15.29	15.52	5.01	5.01	15.68

Table 1 (continued)

Footwall

Sample	RAK 31A							433						
Mineral	gt rim	gt mid	gt core	bt	mus nr gt	mus matrix	ab	mus	ab	bt matrix	bt gt rim	bt in gt	gt rim	gt core
n (analyses)	1	1	1	23	9	7	5	8	8	8	4	11	1	5
Na$_2$O	0.01	0.01	0.03	0.30	1.64	1.58	10.28	0.61	9.46	0.16	0.12	0.22	0.03	0.01
K$_2$O	0.00	0.00	0.00	8.86	8.89	9.01	0.07	10.33	0.21	8.89	9.15	8.48	0.00	0.00
MgO	3.74	3.46	2.37	8.70	0.58	0.69	0.00	1.05	0.00	7.40	7.19	8.58	1.82	2.30
CaO	2.41	2.95	3.76	0.01	0.01	0.00	2.74	0.00	4.03	0.02	0.01	0.06	3.01	3.05
MnO	1.42	1.65	3.66	0.06	0.01	0.00	0.00	0.01	0.00	0.26	0.33	0.12	6.70	4.53
FeO	34.41	34.30	32.60	21.18	2.26	2.35	0.04	21.98	0.02	21.98	22.26	19.28	30.34	32.19
Al$_2$O$_3$	21.35	21.37	21.22	18.60	35.17	34.35	21.76	32.88	22.70	18.09	18.53	18.45	20.24	20.49
SiO$_2$	36.27	35.68	34.30	33.95	44.83	45.08	64.04	46.45	63.86	35.61	35.19	36.43	36.92	37.09
TiO$_2$	0.00	0.02	0.06	1.86	0.36	0.52	0.00	0.88	0.02	3.11	2.48	2.93	0.00	0.02
Total	99.60	99.43	98.00	93.51	93.74	93.59	98.95	94.11	100.30	95.51	95.25	94.55	99.05	99.67
Na	0.00	0.00	0.01	0.09	0.43	0.42	0.89	0.16	0.81	0.05	0.03	0.06	0.00	0.00
K	0.00	0.00	0.00	1.77	1.54	1.56	0.00	1.78	0.01	1.74	1.80	1.65	0.00	0.00
Mg	0.45	0.42	0.29	2.03	0.12	0.14	0.00	0.21	0.00	1.69	1.65	1.95	0.22	0.28
Ca	0.21	0.26	0.34	0.00	0.00	0.00	0.13	0.00	0.19	0.00	0.00	0.01	0.26	0.27
Mn	0.10	0.11	0.26	0.01	0.00	0.00	0.00	0.00	0.00	0.03	0.04	0.02	0.47	0.31
Fe	2.33	2.33	2.27	2.78	0.26	0.27	0.00	0.22	0.00	2.82	2.88	2.45	2.08	2.18
Al	2.03	2.05	2.08	3.44	5.61	5.50	1.14	5.24	1.18	3.27	3.37	3.31	1.95	1.96
Si	2.93	2.90	2.86	5.32	6.07	6.12	2.85	6.28	2.81	5.46	5.44	5.54	3.02	3.01
Ti	0.00	0.00	0.00	0.22	0.04	0.05	0.00	0.09	0.00	0.36	0.29	0.33	0.00	0.00
Total	8.05	8.07	8.10	15.67	14.07	14.06	5.02	13.98	5.00	15.44	15.51	15.32	8.00	8.01

Sample	439							421			
Mineral	bt in gt	bt in gt	bt gt rim	mus	gt rim	gt mantle	gt core	bt	or	gt rim	gt core
n (analyses)	15	4	11	7	1	1	1	24	15	1	1
Na$_2$O	0.33	0.38	0.29	0.97	0.03	0.02	0.00	0.12	1.41	0.01	0.03
K$_2$O	8.85	8.85	8.94	9.79	0.00	0.00	0.00	8.77	14.04	0.00	0.00
MgO	10.30	11.42	8.52	0.74	3.54	4.55	4.15	7.11	0.00	2.68	3.66
CaO	0.05	0.04	0.00	0.01	1.32	1.57	1.36	0.04	0.06	1.97	1.39
MnO	0.04	0.05	0.06	0.01	2.40	1.98	2.57	0.05	0.01	2.39	2.11
FeO	18.32	15.96	20.69	3.16	35.36	34.21	34.51	18.74	0.06	35.27	34.87
Al$_2$O$_3$	19.04	19.21	18.18	33.57	21.40	21.52	21.23	21.21	18.23	20.84	20.66
SiO$_2$	34.82	35.37	35.18	45.86	36.48	37.45	37.30	36.26	66.30	37.62	37.89
TiO$_2$	1.77	1.76	2.77	0.78	0.00	0.02	0.01	3.86	0.01	0.00	0.00
Total	93.52	93.03	94.64	94.90	100.54	101.33	101.14	96.16	100.13	100.78	100.61
Na	0.10	0.11	0.09	0.25	0.00	0.00	0.00	0.04	0.13	0.00	0.00
K	1.74	1.73	1.76	1.68	0.00	0.00	0.00	1.68	0.82	0.00	0.00
Mg	2.37	2.60	1.96	0.15	0.28	0.36	0.33	1.59	0.00	0.32	0.44
Ca	0.01	0.01	0.00	0.00	0.08	0.09	0.08	0.01	0.00	0.17	0.12
Mn	0.01	0.01	0.01	0.00	0.11	0.09	0.12	0.01	0.00	0.16	0.14
Fe	2.36	2.04	2.67	0.36	1.59	1.51	1.53	2.35	0.00	2.36	2.33
Al	3.46	3.46	3.30	5.33	1.35	1.34	1.33	3.67	0.98	1.97	1.94
Si	5.37	5.41	5.42	6.18	1.96	1.97	1.98	5.40	3.02	3.02	3.03
Ti	0.21	0.20	0.32	0.08	0.00	0.00	0.00	0.44	0.00	0.00	0.00
Total	15.62	15.57	15.53	14.04	5.37	5.36	5.36	15.18	4.96	8.00	8.00

Lumla schists

| Sample	RAK 33A				RAK 36			
Mineral	bt	mus	gt rim	gt core	bt	mus	ab	or
n (analyses)	7	7	1	1	16	5	4	3
Na$_2$O	0.17	1.18	0.00	0.02	0.15	0.54	9.61	1.54
K$_2$O	8.61	9.43	0.00	0.00	9.14	10.53	0.22	14.22
MgO	7.19	0.75	2.57	2.58	8.29	0.67	0.00	0.00
CaO	0.02	0.01	0.75	1.65	0.02	0.02	3.94	0.01
MnO	0.11	0.00	1.70	1.73	0.28	0.01	0.01	0.00
FeO	23.33	1.59	37.19	36.43	19.87	2.62	0.24	0.11
Al$_2$O$_3$	18.37	33.50	20.11	20.45	19.21	33.95	22.85	18.75
SiO$_2$	34.69	46.20	36.96	37.02	34.45	45.05	62.21	63.86
TiO$_2$	1.99	0.62	0.00	0.01	2.51	0.69	0.01	0.01
Total	94.47	93.26	99.27	99.89	93.93	94.08	99.10	98.51
Na	0.05	0.31	0.00	0.00	0.05	0.14	0.83	0.14
K	1.71	1.63	0.00	0.00	1.81	1.83	0.01	0.85
Mg	1.67	0.15	0.31	0.31	1.92	0.14	0.00	0.00
Ca	0.00	0.00	0.07	0.14	0.00	0.00	0.19	0.00
Mn	0.02	0.00	0.12	0.12	0.04	0.00	0.00	0.00
Fe	3.05	0.18	2.54	2.48	2.58	0.30	0.01	0.00
Al	3.38	5.36	1.94	1.96	3.51	5.45	1.21	1.03
Si	5.42	6.27	3.02	3.01	5.34	6.13	2.79	2.98
Ti	0.23	0.06	0.00	0.00	0.29	0.07	0.00	0.00
Total	15.54	13.96	8.01	8.02	15.54	14.06	5.04	5.00
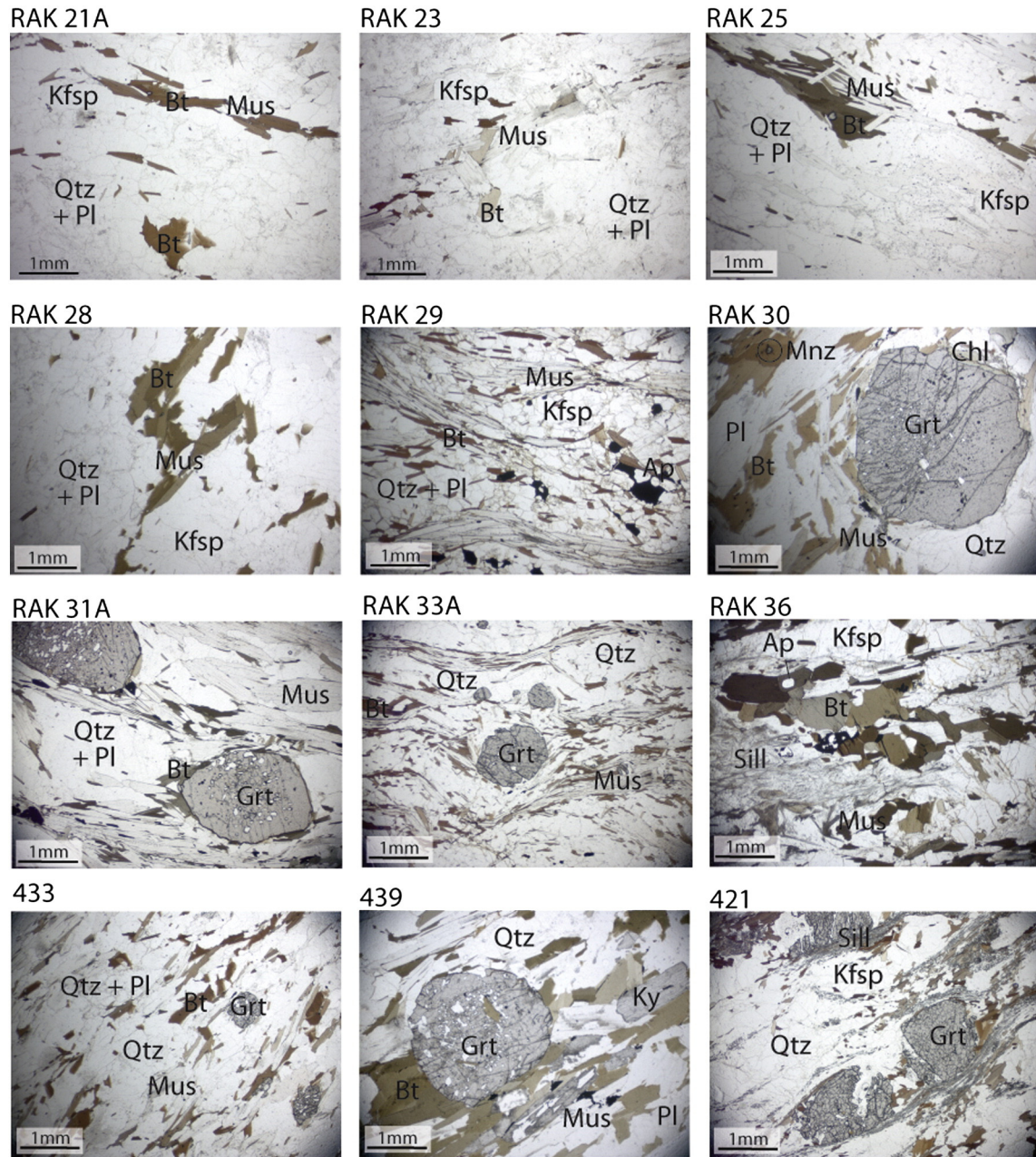
Fig. 2. Thin section photomicrographs of all analyzed samples. Mineral acronyms are from Whitney and Evans (2010): Ap = apatite, Bt = biotite, Chl = chlorite, Grt = garnet, Kfsp = K-feldspar, Ky = kyanite, Mnz = monazite, Mus = muscovite, Pl = plagioclase, Qtz = quartz, Sill = sillimanite. RAK 30 also contains staurolite but it is not shown in this field of view.

Monazite is rare, but where found forms 100–200 μm grains included within biotite and ~50 μm grains included in quartz. Grains show only weak zoning in Y and Th (Fig. A1).

RAK 25 is a weakly foliated gneiss from the hanging wall of the ZT, containing major quartz, plagioclase, K-feldspar, biotite and muscovite with accessory apatite, tourmaline, monazite, xenotime, zircon and opaques. The weak foliation is tightly folded on the cm-scale.

Biotite and muscovite are intergrown as 0.5–1 mm laths, and define the weak fabric. Mica-rich layers are intercalated with plagioclase-rich layers. K-feldspar grains are zoned, yielding compositions that vary from Or_{88} at the rims to Or_{93} in the cores. Plagioclase compositions vary from Ab_{87-95}, but with no consistent core-rim composition trend. Biotites show relatively homogeneous compositions of $X_{Fe} = 0.65$. Muscovites are weakly zoned from core to rim with ~6.3 Si per 22O at the rim and ~6.45 in the core (Fig. 3).

100 μm long monazite grains are associated with plagioclase, biotite and quartz. They show moderate concentric zoning in Th (Fig. A2), with low concentrations in the core and higher concentrations in the rims. In a few grains, a moderate-concentration outer rim is evident. The grains are not zoned in Y. One grain ('5') contains a core of apatite, and a further grain ('6') is intergrown with apatite. This latter grain shows a rim of slightly lower Y concentration than the core.

RAK 28 is a foliated gneiss from the hanging wall of the ZT containing major K-feldspar, plagioclase, quartz, muscovite and biotite, minor garnet and accessory zircon, monazite and apatite. Muscovite forms mm-length laths, whereas biotite forms smaller needles. Muscovite is non-zoned and contains ~6.3 Si per 22O (Fig. 3g). Plagioclase is Ab_{93}, K-fedspar is Or_{92} and biotite has $X_{Fe} = 0.75$.

RAK 29 is a schistose gneiss from within the high strain zone surrounding the ZT containing major muscovite, biotite, plagioclase and
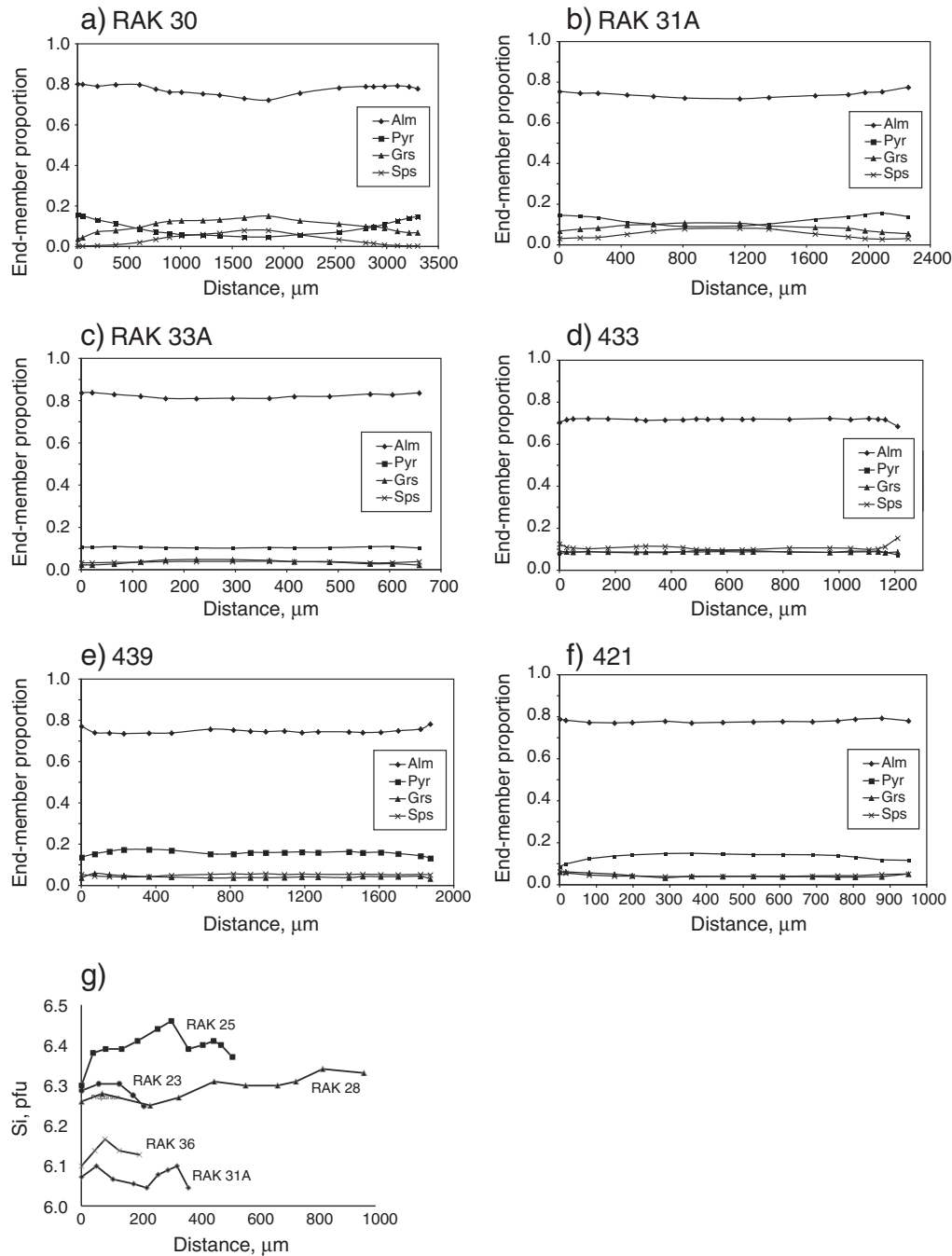
Fig. 3. (a)–(f) Major element profiles across garnet. (g) Si profiles (Si per 22 oxygens) of white micas in samples dated by $^{40}Ar/^{39}Ar$ geochronology.

quartz, with accessory tourmaline, monazite, zircon, baddelyite, xenotime and opaques. Muscovite (containing 6.3 Si per 22O) forms 0.5–1 mm laths in well-defined layers. The grains are commonly rimmed with opaques or biotite, and biotite formation along the cleavages is common. Biotite (X_{Fe} = 0.45) forms smaller needles, and is commonly found in the more mica-poor layers. Plagioclase is Ab_{93}.

Monazite forms as crystals ca. 50 μm in length. Maps of Y concentrations show low-concentration cores and higher concentration rims in some grains; other grains are not zoned (Fig. A3). Xenotime is found as inclusions in monazite cores in some instances (grains '3' and '7'). The zoning mirrors Y zoning: low concentration cores and higher concentration rims in some grains, with limited zoning apparent in others.

RAK 30 is a weakly-foliated garnet-bearing schist from the footwall of the ZT containing major garnet, muscovite, biotite, quartz, and plagioclase, minor staurolite and accessory epidote, allanite, monazite, zircon, apatite, tourmaline, ilmenite and rutile. Garnet rims show evidence for replacement by chlorite during retrogression.

Garnet is almandine-rich and weakly zoned from a core composition of $Alm_{0.72}Pyr_{0.05}Grs_{0.15}Sps_{0.08}$ to a rim composition of $Alm_{0.79}Pyr_{0.13}Grs_{0.08}Sps_{0.00}$ (Fig. 3a). The albite component of plagioclase increases from inclusions in garnet to the matrix, from $Ab_{74–88}$. X_{Fe} in biotite in all structural positions is 0.54, and in chlorite is 0.51. Muscovite contains ~6.2 Si per 22O, and staurolite has Fe/Fe + Mg = 0.83.

Muscovite forms large (1–2 mm) laths as well as smaller crystals. Monazite forms as 100–200 μm-long crystals found in close association with ilmenite, apatite and epidote along grain boundaries and within muscovite, biotite and quartz. Crystals are strongly but irregularly zoned in Y, Th, U and Ce (Fig. A4). High Y rims <5 μm thick are observed

on many grains, with cores showing patches of variable but lower Y concentrations. Th zoning is less concentric. Where monazite is intergrown with apatite, the high-Y rim is discontinuous against the apatite.

RAK 31A is a foliated garnet-bearing schist from the footwall of the ZT, containing major garnet, muscovite, quartz, plagioclase, biotite and accessory monazite, zircon, apatite and tourmaline.

Garnet is almandine-rich and weakly zoned (Fig. 3b) from a core composition of $Alm_{0.72}Pyr_{0.09}Grs_{0.11}Sps_{0.08}$ to a rim composition of $Alm_{0.75}Pyr_{0.15}Grs_{0.07}Sps_{0.03}$. X_{Fe} in biotite in all structural positions is 0.57–0.58. Muscovite near garnet contains 6.07 Si p.f.u. whereas muscovite in the matrix contains 6.12 Si pfu. Plagioclase is Ab_{87}.

1–2 mm muscovite grains show modification to biotite at their rims and along cleavage planes. Muscovite contains inclusions of tourmaline, monazite and zircon.

RAK 33A is a garnet–biotite muscovite schist from the Lumla Window, containing major garnet, biotite, muscovite and quartz with accessory monazite and iron sulfides. Garnet is almandine-dominated, with a core composition of $Alm_{0.81}Pyr_{0.10}Grs_{0.05}Sps_{0.04}$ and a rim composition of $Alm_{0.84}Pyr_{0.10}Grs_{0.02}Sps_{0.04}$ (Fig. 3c). Biotite has $X_{Fe} = 0.65$ and muscovite has 6.27 Si per 22 O.

Monazite grains are generally <100 μm in length and zoned with Y-poor cores and Y-rich rims (Fig. A5). Th concentrations in general decrease toward the rims. Monazite is generally found as inclusions in muscovite, quartz or in the garnet rim.

RAK 36 is a sillimanite-bearing schist from the upper Lumla Formation containing major sillimanite, biotite, muscovite, K-feldspar, quartz and plagioclase with (tiny) accessory monazite, zircon and opaques. Muscovite breakdown to K-feldspar and sillimanite is clearly texturally determinable in some areas of the thin-section, whilst in others muscovite appears to have been replaced by a symplectite of biotite + quartz. Biotite contains $X_{Fe} = 0.57$ in all textural positions, muscovite contains 6.27 Si per 22 O, K-feldspar is Or_{86} and plagioclase is Ab_{81}. 1–2 mm muscovite grains show modification to biotite at their rims and along cleavage planes. Many grains contain abundant sillimanite inclusions. Overall, muscovites are only weakly zoned (Fig. 3g).

Sample 433 is a garnet-bearing schist from the footwall of the ZT, containing major garnet, quartz, plagioclase, muscovite, and biotite, with accessory ilmenite, monazite, apatite and zircon.

Garnets are almandine-dominant, with core compositions of $Alm_{0.72}Pyr_{0.09}Grs_{0.09}Sps_{0.10}$ and rim compositions of $Alm_{0.69}Pyr_{0.07}Grs_{0.09}Sps_{0.16}$ (Fig. 3d). Biotite composition varies according to microtextural position; $X_{Fe} = 0.63$ in the matrix and next to the garnet rim, and between 0.56 and 0.60 as inclusions in garnet. Muscovite has 6.3 Si per 22 O. K-feldspar has a composition of Or_{92} and plagioclase contains Ab_{80}. Monazite grains are between 50 and 100 μm long, and are unzoned in both Y and Th (Fig. A6).

Sample 439 is a garnet-kyanite schist from the footwall of the ZT, containing major garnet, kyanite, quartz, muscovite and biotite with accessory opaques, monazite, zircon and ilmenite.

Garnet compositions are dominated by almandine, and show only minor zoning from a core composition of $Alm_{0.75}Pyr_{0.16}Grs_{0.04}Sps_{0.06}$ to a rim composition of $Alm_{0.77}Pyr_{0.14}Grs_{0.04}Sps_{0.05}$ (Fig. 3e). Some diffusional re-equilibration is evident at the rims. Biotite composition is variable, with $X_{Fe} = 0.44$–0.50 recorded by the inclusions in garnet, and $X_{Fe} = 0.58$ recorded in the matrix next to the garnet rims. Muscovite contains 6.2 Si per 22O.

Monazite is found associated with biotite, both as inclusions within biotite and as grains crystallized along biotite grain boundaries (Fig. A7). The youngest grains (1,3) are unzoned in both Y and Th. Other grains show pronounced Y zoning with high concentrations in grain rims and lower concentrations in the cores. The rims were too narrow (<10 μm) to date.

Sample 421 is a garnet-sillimanite gneiss from the footwall of the ZT, north of Tawang, containing major garnet, quartz, sillimanite, K-feldspar and biotite with accessory apatite, monazite, zircon, ilmenite and rutile. The anhedral habit of the biotite, coupled with intergrowths

of sillimanite and K-feldspar suggest this rock experienced supra-solidus conditions.

Garnets are almandine-dominant, with only minor zoning from a core composition of $Alm_{0.77}Pyr_{0.14}Grs_{0.04}Sps_{0.05}$ to a rim composition of $Alm_{0.78}Pyr_{0.11}Grs_{0.06}Sps_{0.05}$ (Fig. 3f). Biotite has $X_{Fe} = 0.60$ in all microtextural positions within the rock. K-feldspar has a composition of Or_{86}.

Monazite grains are generally 50–100 μm in diameter, with mixed zoning patterns (Fig. A8). One population showed similar zoning in Y and Th: with lower concentration cores, intermediate concentration mantles and 1–2 μm-thick higher Y-concentration rims (grains 3,5,7,8). Other grains showed more patchy, less concordant zoning patterns.

3.1. Thermobarometry

'Traditional' major-element thermobarometric methods were employed in the samples with suitable mineral assemblages (mainly in the footwall of the ZT and the higher-grade Lumla formation samples as the hanging wall samples contained no garnet). Temperatures were estimated using the Fe–Mg exchange between garnet and biotite (calibrations of Bhattacharya et al., 1992; Holdaway, 2000; Holdaway and Lee, 1977) and the garnet–muscovite thermometer (Wu et al., 2002). Garnet–biotite–plagioclase–quartz (GBPQ; Wu et al., 2004) and garnet–plagioclase–muscovite–biotite (GPMB – based on the Holland and Powell, 1998 dataset calibration) geobarometers were used to calculate the pressure in the footwall samples.

The Ti-in-biotite thermometer (TiB) was also used to place constraints on the thermal evolution, despite the estimated pressures being outside the calibrated range (Henry et al., 2005). The precision on the original TiB calibration is estimated at ±12 °C at high temperatures. Here a larger uncertainty (±50 °C) was applied to account for the interpretation that biotite crystallized outside the calibration range of the thermometer (0.3–0.6 GPa).

Hanging wall samples (RAK 21a, 23, 25 and 28) are characterized by variable TiB concentrations and hence temperatures, from 535 to 630 °C (±50 °C, Table 2, Fig. 4). There appears to be no strong correlation between temperature and grain size, although Ti concentrations appear to be positively and linearly correlated with variations in X_{Mg} (Table 2). The ZT shear zone sample, RAK 29, appears to record hotter temperatures of ~680 °C. TiB temperatures yielded by the footwall samples are variable, between 535 and 715 °C but lie in the same range as the hanging wall samples. Temperatures in both hanging and footwalls appear to decrease toward the shear zone (Fig. 4).

4. Geochronology

4.1. Monazite U–Pb

Monazite was dated in situ in polished sections. Each dated grain was mapped for U, Y, Th, Ce and Nd at 1 μm resolution (100 ms per pixel) on the Open University Cameca SX100 EMP prior to dating in order to identify elemental zoning, assist laser spot location and facilitate age interpretation (Figs. A1–A7). Monazite was analyzed using a Nu Instruments AttoM single collector sector-field ICP-MS coupled to a New Wave 193 nm Nd:YAG laser ablation system at the NERC Isotope Geosciences Laboratory (NIGL), in Keyworth, UK; the full method is described in Palin et al. (2013). A New Wave Research 'large format' cell with space for up to eight sample sections was used; this contains an internal ablation cup which provides a washout time of <1 s. A laser spot size of 15 μm at 50–60% laser power and 5Hz yielded a fluence of ~2.0–2.5 J/cm². Samples were ablated for 30s, with a washout time of 10s inbetween each ablation. The masses measured comprise ^{202}Hg, ^{204}Hg + Pb, ^{206}Pb, ^{207}Pb, ^{208}Pb, ^{232}Th and ^{235}U; ^{238}U was calculated using ^{238}U/^{235}U of 137.818 (Hiess et al., 2012).

Data processing for all analyses used the time-resolved function on the Nu Instruments' software, an in-house Excel spreadsheet for data

Table 2
Thermobarometry data.

Sample name	Comment	Ti	X_{Mg}	TiB Temp	Grt Therm.[a]	±	Grt Barom.[b]	±
		apfu		°C	°C	°C	GPa	GPa
RAK 21A	Main foliation	0.28	0.39	630				
RAK 23	Large flakes	0.19	0.31	540				
	Small with ap and mnz	0.22	0.31	580				
RAK 25	Intergrown with muscovite	0.26	0.35	615				
RAK 28	Needles	0.19	0.25	535				
RAK 29		0.33	0.55	680				
RAK 30		0.17	0.46	535	595	40	0.8	0.15
RAK 31A		0.22	0.42	590	595	40	0.9	0.1
RAK 33A		0.23	0.35	590	650	20		
RAK 36		0.23	0.43	630				
433		0.34	0.41	665	635	40	0.8	0.1
439		0.26	0.47	630	690	30		
421		0.46	0.41	715				

[a] Grt–Bt; Grt–Wm.
[b] GBPQ–GPMB.

reduction and uncertainty propagation, and Isoplot for data presentation (Ludwig, 2001). Ratios of Pb/U and Pb/Th were normalized to reference monazite 'Manangotry' (559 ± 1 Ma ID-TIMS age; Palin et al., 2013). A combination of Stern (512.1 ± 1.9 Ma, ID-TIMS age; Palin et al., 2013), 'FC-1' (~56 Ma, ID-TIMS age, NIGL unpublished) and Moacyr (~515.6 ± 1.4 Ma, ID-TIMS age, Palin et al., 2013) monazite reference materials were analyzed during the session with unknowns to monitor data accuracy and precision. Uncertainties were propagated following the procedure of Horstwood (2008) and include a contribution from the external reproducibility of a reference material for the $^{206}Pb/^{238}U$ and $^{208}Pb/^{232}Th$ ratios. The external reproducibility of the $^{206}Pb/^{238}U$ and $^{208}Pb/^{232}Th$ ratios was ~3–4% (2σ) and the accuracy of the ages are within 3% according to measurement of the secondary reference monazite. Analyses were corrected for common lead using either the linear regression suggested by the data, or, where less clear, regressed through a value of 0.83 ± 0.02 (equivalent at ~20 Ma to Stacey and Kramers, 1975); this composition was validated using measurement on feldspars in some samples. The effect of possible excess ^{206}Pb was corrected for using a whole-rock Th–U ratio of 3, and was negligible for these samples. The analytical protocol is designed to provide maximum precision on the U–Pb ages, rather than the Th–Pb ages, therefore the latter are provided but not used for discussion of the ages. Results are summarized in Table 3 and
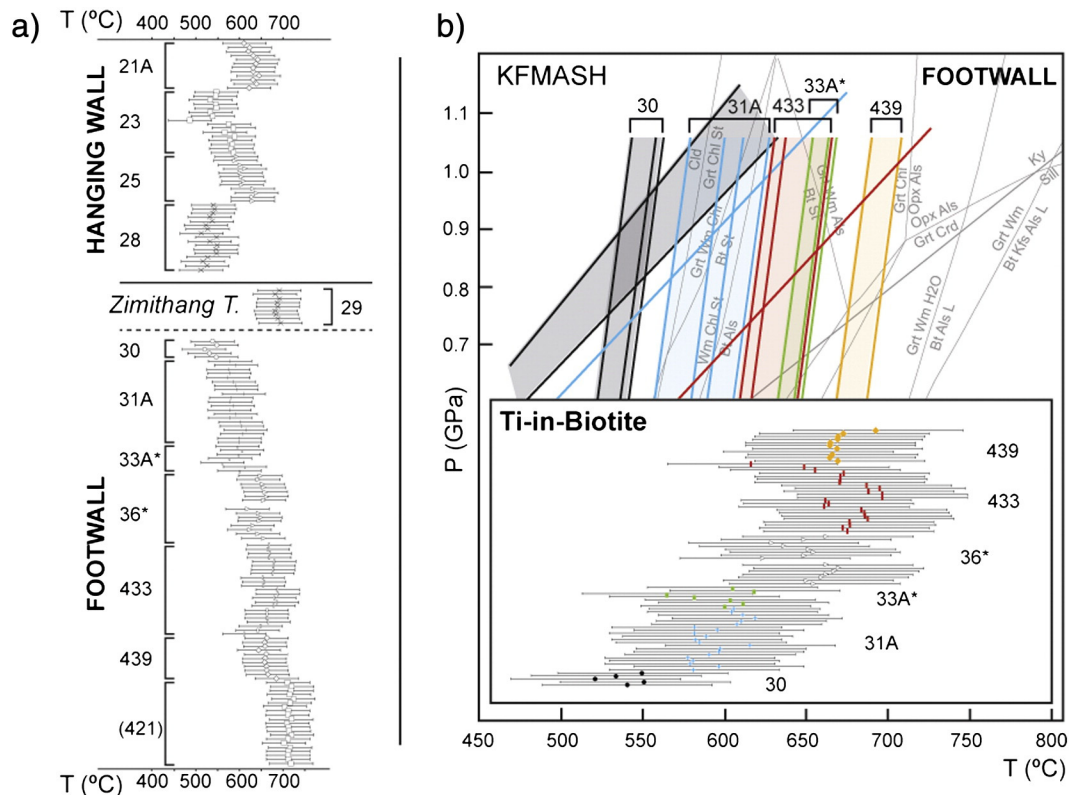

Fig. 4. (a) Titanium-in-biotite (TiB) temperatures per sample in the hanging and footwalls of the ZT. Each datapoint is a single analysis (full data table in supplementary data). The brackets around sample 421 represent the uncertainty about its structural position with respect to the ZT compared to the other samples. Samples RAK 33A and 36 (marked with a *) are sampled from the Lumla Formation. (b) Garnet–biotite thermobarometry data. Garnet was only present in the footwall assemblages. The Grt–Bt temperatures are similar to the TiB temperatures, attesting to the robustness of the thermometer even outside its calibrated pressure range.

Table 3
Summary geochronology data.

Monazite U–Pb	Hanging/footwall	Max age	±	MSWD	Min age	±	MSWD	Inherited age	±
		Ma	Ma		Ma	Ma		Ma	Ma
RAK 21A	Hanging wall	15.47	0.18	0.80	–	–	–	–	–
RAK 23	Hanging wall	15.38	0.55	7.8	–	–	–	–	–
RAK 25	Hanging wall	16.02	0.17	1.2	12.68	0.36	0.55	–	–
RAK 29	Shear zone	14.91	0.28	1.16	11.52	0.32	0.75	836 and 625	–
RAK 30	Footwall	20.79	0.6	0.21	15.52	0.44	1.5	–	–
421	Footwall	19.11	0.4	2.2	–	–	–	–	–
433	Footwall	17.14	0.21	2.6	–	–	–	548	7.5
439	Footwall	27.27	0.56	1.6	18.03	0.26	0.44	–	–

Muscovite Ar/Ar		Max age	Min age	Wt avg.	±	MSWD	Intercept age	±	MSWD	atm intercept?	Initial $^{40}Ar/^{36}Ar$
		Ma	Ma	Ma	Ma		Ma	Ma			
RAK 21A	Hanging wall	9.29	6.35	7.32	0.55	1.5	7.37	0.85	0.66	y	269 ± 83
RAK 23	Hanging wall	7.57	5.91	6.90	0.36	2.2	6.90	1.80	3.10	y	286 ± 120
RAK 25	Hanging wall	7.81	5.63	7.04	0.18	1.0	6.87	0.35	1.30	y	313 ± 37
RAK 28	Hanging wall	10.97	8.42	8.98	0.33	1.3	9.30	1.20	8.00	y	294 ± 110
RAK 31A	Footwall	8.33	6.38	7.32	0.33	1.4	7.29	0.67	2.20	y	290 ± 35
RAK 36	Footwall	15.71	8.31	11.50	1.50	13	12.47	0.75	1.70	n	–

Biotite Ar/Ar									
RAK 21A	Hanging wall	13.80	9.48	11.10	1.00	8.8	n/a		
RAK 23	Hanging wall	18.28	8.21	9.45	0.90	4.6	n/a		
RAK 25	Hanging wall	10.58	8.54	9.58	0.89	4.7	n/a		
RAK 28	Hanging wall	20.09	15.26	17.90	3.00	29	n/a		
RAK 31A	Footwall	10.16	7.98	8.59	0.84	2.2	n/a		
RAK 36	Footwall	19.63	15.29	17.10	2.20	12	n/a		

plotted in Figs. 5 and 6; full data are in Supplementary Data Table A1. Monazite location BSE images, elemental zoning maps in Y and Th of each dated grain and laser analysis spot locations are presented in Supplementary Figs. A1–A7.

Ten spots on three grains from hanging wall sample RAK 21a yielded an age population of 15.5 ± 0.2 Ma (Fig. 5). One grain yielded a non-reproduced, slightly younger age, which is documented but ignored in the discussion. The single yielded population is consistent with the lack of zones of different chemistry in the monazite grains.

Eleven spots on four grains from hanging wall sample RAK 23 define a mixed population. Three spots on two grains yield an older population at ca. 17 Ma, and four spots on two grains yield a younger population at ca. 14 Ma (Fig. 5). Four further analyses yield intermediate ages. The chemical zoning in Y and Th in these grains is weak, and no obvious link between age and mineral chemistry could be determined from the grain maps and spot locations (Fig. A1).

Nineteen spots on nine grains from hanging wall RAK 25 yielded two age populations at 16.0 ± 0.2 Ma (11 spots on seven grains) and 12.7 ± 0.4 Ma (four spots on four grains, Fig. 5). Four further spots yielded mixed ages between these two populations. No notable links were observed between the yielded ages and zoning in Y or Th (Fig. A2), although the youngest yielded ages were always from rim portions.

Seven spots on nine grains from RAK 29, within the Zimithang Thrust shear zone, yielded an intercept age of 14.9 ± 0.3 Ma, and three spots on one grain ('8') yielded an intercept age of 11.5 ± 0.3 Ma (Fig. 5). Three populations of concordant "detrital" ages were also yielded from this sample at ~850 Ma (four analyses), ~625 Ma (two analyses) and ~550 Ma (one analysis). Ten further analyses yielded mixed ages between the concordant detrital cores and the younger Himalayan overgrowths. No obvious link was determinable between age and monazite chemistry. The low-Y cores of some of the grains yield pre-Himalayan ages, but other cores with similar chemistry yield Himalayan ages. Grains 6, 7, and 8 show higher Y concentrations but do not yield an obvious age population (Figs. 5 and A3).

Twenty two spots on ten grains from footwall sample RAK 30 yielded two age populations at 20.8 ± 0.6 Ma (nine spots on four grains) to 15.5 ± 0.4 Ma (four spots on three grains, Fig. 5). A further 8 analyses yielded ages that plotted between these two populations. There is no

obvious link between monazite age and chemistry: the youngest age population (yielded by spots on grains 3, 6 and 7) is yielded by zones that are chemically similar to zones that yield the older age population (Fig. A4).

Monazite occurrence in Lumla Formation sample RAK 33a was rare, and grains were generally only 20–50 μm in diameter. Nine spots on six grains from RAK 33a yielded a scattered mix of dates that did not yield a systematic age population (Fig. A5).

Twenty eight spots on nine grains of footwall sample 433 define a single age population at 17.14 ± 0.21 Ma (MSWD = 2.6, Fig. 6). One grain ('g') contains high common lead concentrations and plots off this trend, as do three other analyses (marked with a * in Supplementary Table A1). The single yielded population is consistent with the unzoned monazite chemistry (Fig. A6).

Fourteen spots on five grains from footwall sample 439 define a scattered dataset. Two spots from grain '2' define an older population at 27.3 ± 0.6 Ma, and five spots on two grains (four on grain '1' and the whole of grain '3', which is included in garnet and was too small to be mapped, Fig. A7) define a younger population at 18.0 ± 0.3 Ma (Fig. 6). Further spots yield intermediate ages. Grain '1' was unzoned, with intermediate Y concentrations compared to the Y zoning mapped in grains '2' and '5' (Fig. A7). The oldest ages were yielded from low-Y cores in grain '2'; with possibly a mixed population yielded from narrow high-Y rims.

Twenty eight spots on eight grains from footwall sample 421 yielded two distinct age populations. Four spots from core of grain '6' yielded an upper intercept age of 548 ± 7.5 Ma (Figs. 6 and A8). Thirteen spots on four grains yielded a younger 'Himalayan' intercept age of 19.1 ± 0.4 Ma. Six further spots yield mixed ages between the inherited and 'Himalayan' age populations. Monazite grains that yield the Himalayan ages are zoned in Y, with generally lower concentration cores (blue in Fig. A8), intermediate mantles (green) and narrow, patchy high concentration rims (red). Grain '3' also yielded a high Y concentration inner mantle. There appeared to be no notable difference between the ages yielded from the different zones, although the intermediate mantles appear to contain less common lead than the cores.

In summary, samples in the hanging wall and high strain zone of the Zimithang Thrust yield 'Himalayan' age populations from 17 to 11.5 Ma,
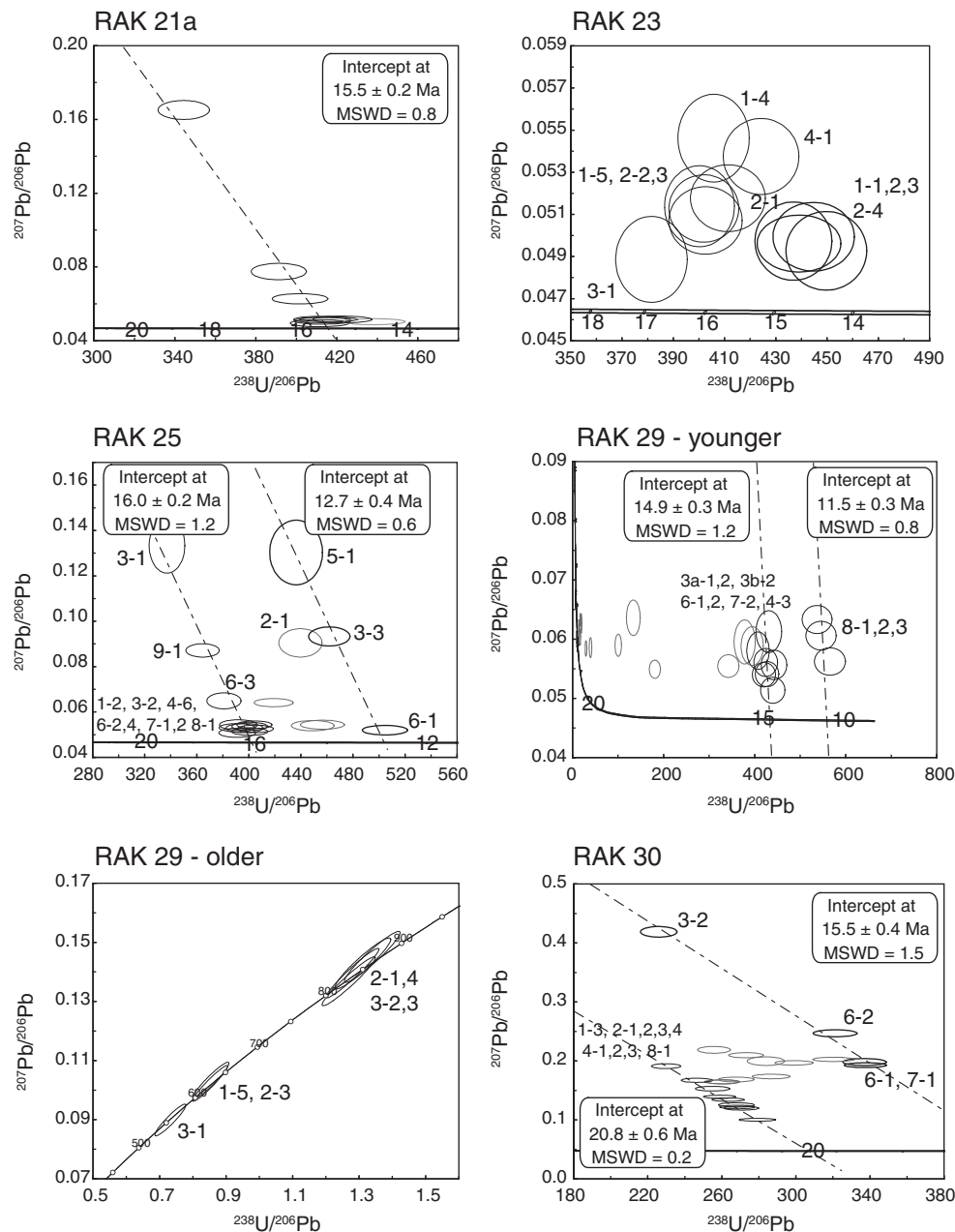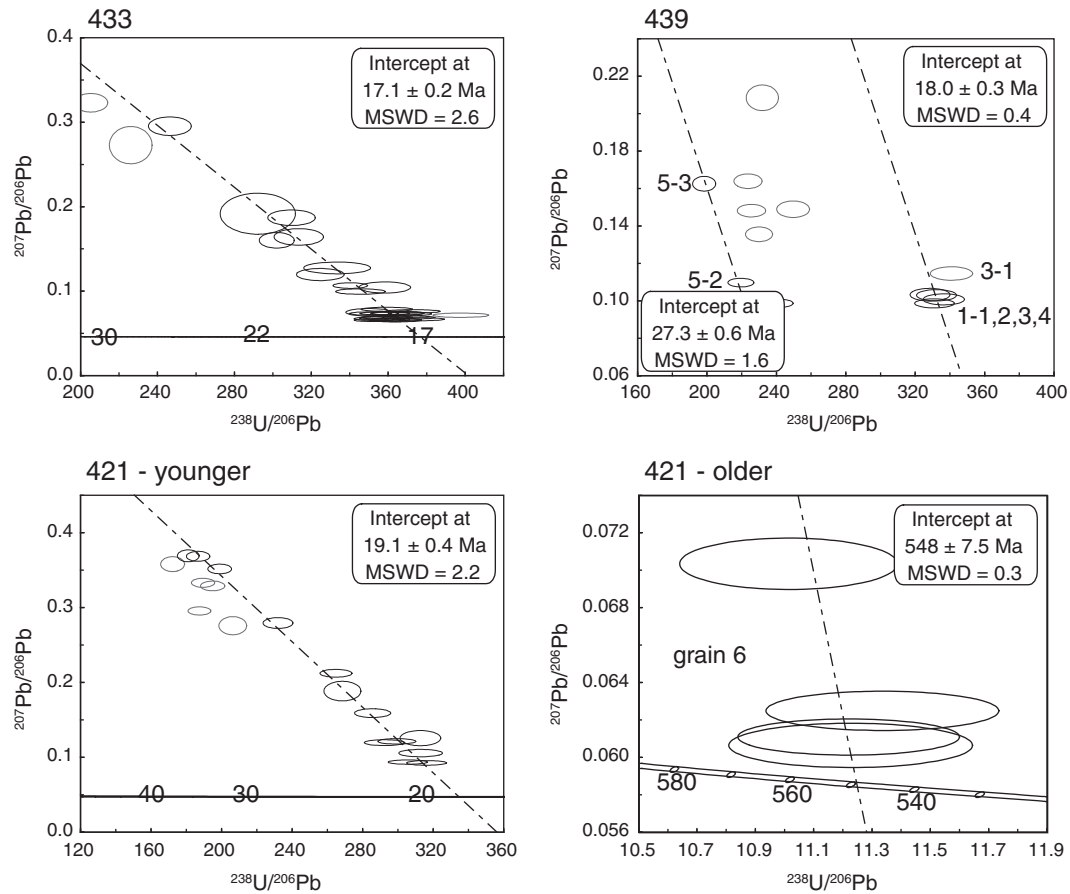
Fig. 5. U–Pb data for monazite in samples 21A through 30. Labels next to ellipses refer to the analyses numbers (full data tables in Supplementary data). Common-lead regressions were drawn through the data where it was considered robust to do so.

with inherited cores of ca. 850, 625 and 550 Ma. Samples from the foot-wall schists and gneisses yield older ages between 27 and 15.5 Ma. A single inherited grain from a footwall sample yielded an age of ca. 550 Ma.

4.2. $^{40}Ar/^{39}Ar$ geochronology

Six samples from a transect spanning the Zimithang Thrust (samples RAK 21A, 23, 25, 28, 31A and 36) were analyzed for their muscovite and biotite $^{40}Ar/^{39}Ar$ ages in order to determine the timing of juxtaposition of hanging and footwall terranes across the structure. Single muscovite grains were separated from crushed, washed and sieved samples. The largest (see Sample Description section for size ranges), least-deformed, most inclusion-free muscovites were picked from each

sample. Grains were washed in acetone, methanol and water before packing into foil packets for irradiation.

Samples were irradiated at McMaster University in Canada and ana-lyzed in the Open University $^{40}Ar/^{39}Ar$ Laboratory. Irradiation flux was monitored using the GA1550 biotite standard with an age of 98.79 ± 0.54 Ma (Renne et al., 1998). The following correction factors were applied to the biotite standards: $(^{39}Ar/^{37}Ar)Ca = 0.00065$, $(^{36}Ar/^{37}Ar)Ca = 0.000265$, $(^{40}Ar/^{39}Ar)K = 0.0085$ based on analyses of Ca and K salts; only the K correction was applied to the analyzed muscovites. Sample J values were calculated by linear interpolation between two bracketing standards (J values are given in Supplementary Table A2); a standard was included between every 8–10 samples in the irradiation tube. The decay constants of Steiger and Jäger (1977) were used to calculate the ages.

Fig. 6. U–Pb data for monazite in samples 421–439. Labels next to ellipses refer to the analyses numbers (full data tables in Supplementary data). Common-lead regressions were drawn through the data where it was considered robust to do so.

Samples were loaded into an ultra-high-vacuum laser port and placed under a heat lamp for 8 h to reduce atmospheric blank levels. Total fusion of single grains was achieved using a Nd-YAG 1064 nm infra-red (IR) laser coupled to an automated gas handling vacuum system and admitted into an MAP 215–50 noble gas mass spectrometer. Inlet gas was gettered using two SAES getters (at 450 °C and room temperature) and a liquid nitrogen cold trap provided additional gas-cleaning. Peaks from ^{36}Ar to ^{40}Ar were scanned 10 times each and amounts were extrapolated back to the inlet time.

Background measurements bracketed every 1–2 sample measurements. Average background measurements are presented in Supplementary Table A2, tabled data are background corrected. Analyses were corrected for mass spectrometer discrimination, using a value of 283 (determined from analyses of modern glass).

In common with other small-volume studies, ^{36}Ar sample and background measurements approached detection limits, and were commonly within error of each other. The correction for atmospheric argon magnifies errors on the ^{36}Ar measurement and results in anomalously high analytical errors on the final $^{40}Ar/^{39}Ar$ age (Sherlock et al., 2005). Samples were only corrected for atmospheric argon where the ^{36}Ar measurement was >2× the ^{36}Ar background and outside the blank measurement uncertainty (indicated in Supplementary Table A2). The uncertainty on the calculated age for uncorrected samples was doubled in compensation (Warren et al., 2011b; Sherlock et al., 2005, 2008; Warren et al., 2012a). Whilst not a strictly rigorous way of estimating the uncertainty on each analyzed age, it is probably a more realistic uncertainty of the error than the uncertainty calculated without

atmospheric correction. Data were reduced using an in-house software package (ArMaDiLo) developed by James Schwanethal.

In general, muscovites from five of the dated samples (RAK 21A, 23, 25, 28, and 31A) yielded narrow ranges of single grain fusion ages that yielded statistically identical weighted average ages ranging from 6.90 ± 0.36 Ma to 8.98 ± 0.33 Ma (MSWD values range from 2.20 to 0.98; Fig. 7a and Table 3). Isochron regressions of the samples yielded ages that were identical within error (Fig. A9). One sample, RAK 36, yielded a wider range of older ages, with a weighted mean average age of 11.50 ± 1.5 Ma.

Biotites from the same samples yielded older ages than the muscovites, with wider ranges. The youngest biotite age commonly only overlaps within error with the oldest muscovite age (Fig. 7b). Isochron regressions showed no extra insight (Fig. A9).

5. Discussion

5.1. Thermobarometry

In all of the samples, biotite is interpreted (from textural and chemical evidence) to be stable at peak thermal conditions, suggesting that the temperatures they yield provide a reliable estimate of peak temperature. The different thermometers used for determining equilibrium temperatures in the footwall samples agree best for the lowest and highest temperature samples 30, 31A and 439. In sample 433 the TiB data yield slightly higher temperatures than the Grt–Bt data, whereas in sample 33A the TiB data yield lower temperature. Overall, though, the different thermometers agree within error (Fig. 4b).
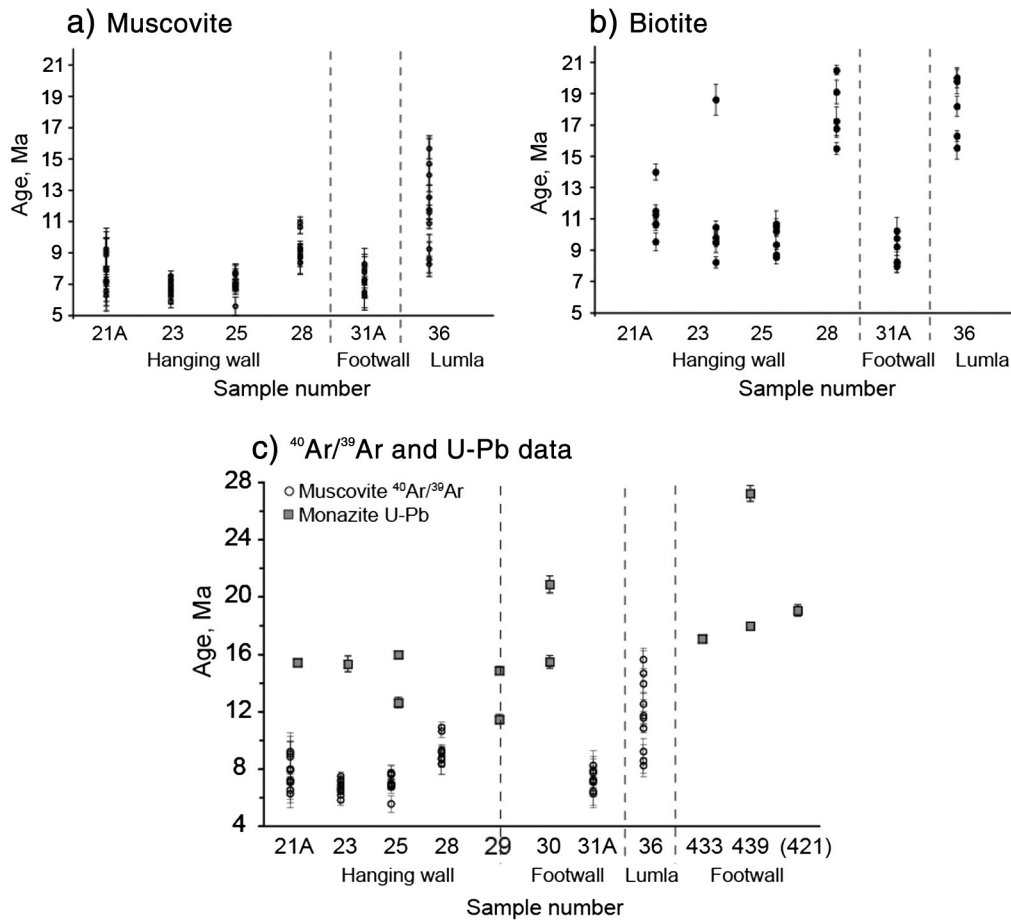
Fig. 7. Single-grain fusion $^{40}Ar/^{39}Ar$ data from (a) muscovite and (b) biotite. Each data point represents the age yielded by completely melting a single grain. (c) $^{40}Ar/^{39}Ar$ muscovite and monazite U–Pb ages plotted together. Overall the youngest U–Pb ages in the hanging wall are younger than the youngest ages in the footwall. The $^{40}Ar/^{39}Ar$ data do not show a significant change in age across the Zimithang Thrust. The brackets around sample 421 represent the uncertainty about its structural position with respect to the ZT compared to the other samples.

The overall agreement between the different methods suggests that our self-imposed 50 °C uncertainty on the TiB temperatures to account for our application of the thermometer outside the calibrated range is sensible, and also that the temperatures determined for the hanging wall, in garnet-absent lithologies, are robust. The 50 °C uncertainty estimate also covers the sample-specific uncertainty in Ti activities relating to the presence of ilmenite or rutile; these buffer the within-sample Ti concentrations.

5.2. The timing of high-T metamorphism

Our new U–Pb LA–ICP–MS monazite data from Arunachal Pradesh show that monazite in metamorphic rocks exposed in the hanging wall of the Zimithang Thrust yield younger ages (17–11.5 Ma) than those in the footwall (27–15.5). These ages, and the northwards decrease in ages across the structure, are similar to those reported from monazite and zircon across the Kakthang Thrust in NW Bhutan (~15–13 Ma in the hanging wall and 21–17 Ma in the footwall; Warren et al., 2011a; Grujic et al., 2011), and younger, but showing a similar trend to ages reported at the highest structural levels of Sikkim (Kellett et al., 2013; Rubatto et al., 2013). This structurally-upwards younging trend is opposite to that reported from central and eastern Nepal (Corrie and Kohn, 2011; Imayama et al., 2012).

Like many other in-situ LA–ICP–MS U–Pb monazite data reported from across the Himalaya, our results show that many samples yield a range of ages that spread across ~3–9 Ma. It is often unclear as to whether this scatter is due to two or more different monazite crystallization

events, with intermediate ages reflecting population mixing due to analysis, or whether the scatter represents continuous monazite crystallization recorded in that sample. In general, recent studies suggest that the most coherent populations are yielded from the largest, most coherent monazite zones, with more scattered populations yielded from narrow rim zones (e.g. Greenwood, 2013). This suggests that the scatter in the data is most likely caused by analytical mixing between two age populations rather than continuous crystallization — a conclusion that appears to be supported by the data in this study. Visual inspection of the position of the laser pits on the grain surface does not always aid interpretation due to the irregular nature of the zone boundaries below the grain surface.

The dated monazite-bearing gneiss in the hanging wall of the ZT (RAK 21, 23, 25, 29) contain major K-feldspar, plagioclase, quartz, muscovite and biotite, with no garnet. Because of the limiting assemblage, the precise PT evolution of the bulk rock and conditions at which the monazite (re)crystallized remains unconstrained. The collection of monazite trace element data to allow their relative timing of crystallization to be linked to the evolution of the main rock-forming minerals, (e.g., Regis et al., 2014; Rubatto et al., 2013) was outside the scope of this study.

The monazite grains in the hanging wall are all included in biotite or are found along biotite grain boundaries. There is no relationship between U–Pb age and textural position in sample RAK 21 – all monazite grains yield the same age regardless of whether they are included in biotite or quartz. In samples RAK 23 and RAK 25, older monazite ages are yielded by inclusions in quartz, but zoned grains yielding both the older

(~16 Ma) population and the younger (~13 Ma) populations are found as inclusions in biotite. This suggests that the ages recorded by monazite in the hanging wall gneisses record the timing of prograde to peak metamorphism.

Sample RAK 29, in the shear zone itself, yields some of the highest temperatures (~680 °C) and the youngest ages (~15–11.5 Ma) in this sample set. The 'older', ~15 Ma ages are yielded by monazite grains in quartz and found along the qtz-bt grain boundary. The youngest, ~11.5 Ma, ages are all yielded by a single monazite included in biotite. We therefore interpret the ~15–11.5 Ma dataset to record the timing of the latest stage of fabric growth in the shear zone. The high temperatures might be caused by equilibration in the presence of hot fluids percolating through the shear zone. Shear heating is considered less likely as heating this way would need very strong rocks, the effects would be highly localized (mm-scale), and generated heat would probably dissipate rapidly (e.g. Jamieson and Beaumont, 2013). The presence of fluids is also suggested by the elevated $^{40}Ar/^{39}Ar$ age signature in nearby sample RAK 28.

The footwall schists contain garnet and biotite and are therefore more amenable to PT condition determinations by multiple different thermobarometers. Textural relationships between monazite and the major rock-forming minerals at least partly constrain the temporal evolution in the area. In RAK 30 the timing of garnet rim growth is constrained by the ages of monazite inclusions at 20.8 ± 0.6 Ma, providing constraints on near-peak conditions. Further monazite crystallization in the matrix, possibly during exhumation, occurred until at least 15.5 ± 0.4 Ma. In sample 421, monazite yielding a single age population and texturally associated with biotite and sillimanite and K-feldspar, suggests high grade metamorphism at 19.1 ± 0.4 Ma (in this sample TiB temperatures were >700 °C). In sample 439, a single small monazite included in the garnet mantle, and a larger grain in the matrix yielded ages of 18.0 ± 0.3 Ma, suggesting that garnet was growing until at least 18 Ma in this sample. All the other matrix monazite grains in this sample yielded older or mixed ages with a maximum of 27.3 ± 0.6 Ma, potentially recording protracted monazite growth during prograde metamorphism. 433 yielded a younger, single population at 17.1 ± 0.2 Ma. In this sample the monazite grains were all in the matrix, associated with muscovite, biotite and quartz. We interpret the ages as recording the timing of fabric mineral growth in this sample.

In summary, therefore, prograde garnet growth in the footwall is constrained between ~21 and 18 Ma in multiple samples. Monazite crystallization lasted until at least ~15.5 Ma, however narrow (~5 μm) monazite rims with enriched Y or Th concentrations, which were too narrow to analyze in polished cross-section, attest to continued monazite crystallization after ~15.5 Ma.

5.3. The timing of cooling

$^{40}Ar/^{39}Ar$ muscovite and biotite data are commonly used to constrain the timing of cooling and exhumation in metamorphic rocks, via the assumption that ^{40}Ar produced by radioactive decay in the mica will be lost via thermally-activated diffusion at high temperatures (e.g. McDougall and Harrison, 1999). Experimental data and data from natural samples suggest that diffusion will operate efficiently to lower temperatures in biotite than in muscovite (Dodson, 1973; Harrison et al., 1985, 2009).

Across our samples, the biotites systematically yield older ages than the muscovites. This 'inversion' of ages appears to be common across the Himalaya at all structural levels (e.g. Copeland et al., 1991; Stüwe and Foster, 2001; Viskupic et al., 2005). From closure temperature considerations, older biotite ages suggest the presence of excess Ar (^{40}Ar decoupled from parent ^{40}K), potentially inherited from an Ar-rich fluid during deformation and cooling. The biotite data do not plot as a linear isochron on an inverse isochron plot, therefore the data yield no insight about the composition of the contaminating Ar. (Suppl Figure A9).

The suggestion of excess Ar in biotite means the interpretation of the younger muscovite ages as representing geologically-meaningful cooling ages should also be carefully assessed. Inverse isochron regressions for muscovite suggest a reasonable mixing trend between atmospheric Ar ($^{36}Ar/^{40}Ar$ ratio of ~0.003) and a radiogenic component. The inverse isochron ages are generally indistinguishable from the weighted mean ages (Table 3). Under these criteria, therefore, the muscovite ages appear to be more robust (and geologically reliable) than the biotite ages.

Each sample yields variable muscovite age dispersion, from 1.7 Ma (RAK 23) to 7.4 Ma (RAK 36). This dispersion is greater than analytical uncertainty, which on the GA1550 standards is ~0.5%. A scatter of ~0.04 Ma would therefore be expected from analytical uncertainty in an 8 Ma sample. The observed dispersion could be caused by variability in diffusion (commonly equated to grain) radius or by subtle variations in concentrations of radiogenic vs. non-radiogenic argon hosted by the mineral.

Under the assumption that simple volume diffusion is the main mechanism for argon redistribution in samples (and this is commonly questioned in metamorphic rocks, see for example Villa, 1998), a variation in diffusion radius from 0.5 to 1 mm (similar to the picked grain sizes) would be responsible for a ~1 Ma difference in age if cooled linearly from 650 °C at 25 °C Ma^{-1}, a ~2.5 Ma difference in age if cooled linearly at 10 °C Ma^{-1}, and a 4–5 Ma difference in age if cooled linearly at 5 °C Ma^{-1} (modeled using the Wheeler (1996) program 'DiffArg' and the Harrison et al. (2009) diffusion parameters for muscovite at 10 kbar (the pressure of experimental calibration); see Warren et al., 2012b for details). A smaller dispersion would be expected for an exponentially-decreasing cooling rate. The majority of the samples in this study show muscovite age dispersions of <3 Ma, suggesting that variations in picked grain size and effective diffusion radius could be responsible for most of the measured dispersion.

Heterogeneously incorporated excess argon or grain-scale variations in argon loss due to recrystallization could also disturb the diffusion-related argon systematics. Chemical and textural evidence suggests a single generation of mica in each sample, with minimal chemical zoning in the muscovite (Fig. 3g). These data preclude inheritance of detrital muscovite cores. As discussed above, the majority of the samples show age dispersions that are commensurate with variability in picked grain size, with possibly a small contribution from some excess argon. The 7.2 Ma dispersion and the oldest age range yielded by sample RAK 36, however, is beyond the expected range, therefore we feel that it is likely that the muscovites in this sample are contaminated with excess argon. This particular sample was collected from within the Lumla window, but further work is needed to understand the cause of the contamination.

Overall, the weighted averages of the ages yielded by the hanging wall samples (RAK 21A, 23 and 25) and the 'reliable' single footwall sample (RAK 31A) form a tight cluster at 6.9–7.3 Ma. RAK 28 forms a slight outlier, yielding a weighted average age of 9 Ma; this sample is close to the ZT shear zone so may have been exposed to Ar-rich fluids within the shear zone itself. Diffusion models using Diffarg show that an $^{40}Ar/^{39}Ar$ age of ~7 Ma may be yielded by cooling from ca. 600 °C at 13 Ma (youngest monazite in hanging wall sample RAK 25) at a linear rate of ca. 15–20 °C Ma^{-1}.

Our new single-grain fusion muscovite $^{40}Ar/^{39}Ar$ ages are similar to previously reported regional step-heating plateau ages from the same region (Yin et al., 2010). Experiments have shown that weighted mean ages of a single grain fusion dataset are within uncertainty of the plateau ages yielded by multi-grain aliquots from the same sample (Warren et al., 2012c). The Yin et al. (2010) analyses yielded muscovite step-heating plateau ages of 12.3 ± 0.3 and 7.7 ± 0.2 Ma in the hanging wall of the ZT, and 11.0 ± 0.2 and 8.0 ± 0.3 Ma in the footwall. They suggested that these ages showed an increase in muscovite $^{40}Ar/^{39}Ar$ age with increasing distance from the ZT. Our more comprehensive dataset shows no such clear trend, and shows no variation in age across the ZT in this region (Fig. 1). This suggests that the hanging and footwall of

the ZT were juxtaposed at temperatures that still allowed efficient Ar diffusion in muscovite.

Our analyses yield muscovite ^{40}Ar/^{39}Ar ages that are younger than those yielded by similar muscovite grain size fractions from granites and gneisses at similar structural levels along strike further to the west in Bhutan (~11 Ma; Maluski et al., 1988), Sikkim (~13 Ma; Kellett et al., 2013), and the Everest region in Nepal (~15 Ma; Carosi et al., 1998). This trend suggests either later or slower cooling from the central to the eastern Himalaya.

5.4. Out-of-sequence thrusting in the GHS

One of the major current working models by which at least the high-temperature part of the exhumation of the Greater Himalayan Sequence is explained, suggests that weak, partially molten material from mid orogenic crustal levels was transported to the surface along two coeval, opposite-sense shear zones: the South Tibetan Detachment and the Main Central Thrust (e.g. Beaumont et al., 2001). In this model, no other major structures disrupt or facilitate this 'channelized' flow of material. Increasing amounts of data from the Greater Himalayan Sequence, however, suggest that significant PTt discontinuities exist within the GHS, suggesting that in detail, exhumation was not as smooth and continuous as the current models suggest (e.g. Warren et al., 2011a; Corrie and Kohn, 2011; Gansser, 1983).

These discontinuities within the GHS appear to have formed as thrust-sense structures, both 'in-sequence', such as the Sinuwa and Banuwa Thrusts in Nepal, where older, higher-grade metamorphic rocks are thrust over younger, lower-grade rocks (e.g. Corrie and Kohn, 2011) and 'out-of-sequence', such as the Laya–Kakthang–Zimithang Thrust system, where younger, higher-grade metamorphic rocks are thrust over older, lower-grade rocks (e.g. Warren et al., 2011a; Gansser, 1983; Grujic et al., 2011; Yin et al., 2010).

In Bhutan, the Laya Thrust juxtaposed the hanging and footwalls by at least 10 Ma (U–Pb rutile, Warren et al., 2011c), whereas in Arunachal Pradesh, ^{40}Ar/^{39}Ar data suggests that motion along the Zimithang Thrust had stopped by at least 7 Ma (this study). These datasets imply that if the Laya–Kakthang–Zimithang system is continuous, then it was operating as motion along the structurally lower Main Central Thrust ceased (motion is constrained by U–Pb monazite data between ~21 and 9 Ma in Sikkim, Mottram et al., 2014, ~21–15 Ma in W. Bhutan, Tobgay et al., 2012, and ~22–16 Ma in E. Bhutan, Daniel et al., 2003). There are only sparse data constraining the timing of motion along the South Tibetan Detachment in the eastern Himalaya, with motion constrained between ~24–13 Ma in Sikkim and ~26–15 Ma in W. Bhutan (Kellett et al., 2009, 2013 respectively).

The tectonic mechanism for transporting material along the Laya–Kakthang–Zimithang structure is therefore still somewhat unclear. One option, supported by thermo-mechanical numerical model results (Model HT 111; Beaumont et al., 2006; Jamieson et al., 2006) is that deep crustal material was forced surface-wards over an incoming 'ramp' of stronger Indian crust. INDEPTH reflectors appear to show a ~35 km-high ramp in the Main Himalayan Thrust under the present-day Kangmar Dome (Hauck et al., 1998). A similar structure may have been responsible for the exhumation of the rocks now exposed in the hanging wall of the Laya–Kakthang–Zimithang thrust system (Warren et al., 2011a; Grujic et al., 2011; Kellett et al., 2010). Similar 'plunger' mechanisms have been suggested for other tectonic settings, including subduction zones (Warren et al., 2008).

6. Conclusions

Monazite U–Pb data from rocks in the hanging and footwalls of the Zimithang Thrust at high structural levels of the Greater Himalayan Sequence in Arunachal Pradesh, NE India show that the structure juxtaposes younger (~17 to 12.7 $\pm$ 0.4 Ma) rocks in the hanging wall over older (27.3 $\pm$ 0.6 to 17.1 $\pm$ 0.2 Ma) rocks in the footwall. Monazite

grains in hanging wall rocks are included in biotites that yield titanium-in-biotite temperatures between ~535 and 630 °C, suggesting near-peak conditions for monazite growth. Monazite grains included in garnet in footwall rocks constrain the timing of garnet growth to ca. 21 Ma, with further monazite crystallization until 17.1 $\pm$ 0.2 Ma. Monazite from a sample collected in the shear zone itself grew in association with fabric-forming biotite between 14.9 $\pm$ 0.3 and 11.5 $\pm$ 0.3 Ma at temperatures of ~680 °C.

Single grain fusion ^{40}Ar/^{39}Ar muscovite data from samples across the same transect yield youngest ages of ~7 $\pm$ 0.5 Ma. Together the ^{40}Ar/^{39}Ar and U–Pb data suggest that the ZT had juxtaposed the hanging and footwalls between ~11.5 and 7 Ma, at temperatures higher than the closure temperature for Ar diffusion in muscovite.

The new data lend strength to the suggestion that the Zimithang Thrust is the eastwards continuation of the out-of-sequence Laya and Kakthang Thrust mapped in Bhutan. This structure consistently appears to juxtapose younger metamorphic rocks on top of older metamorphic rocks, although the pressure–temperature variation across the structure is not as pronounced as in Bhutan.

The new data, in conjunction with those previously published, suggest that the South Tibetan Detachment facilitates exhumation of GHS material from different structural levels with differing high-temperature histories at different times. U–Pb ages of rocks at the highest structural levels of the GHS broadly decrease from central Nepal to Arunachal Pradesh, but peak metamorphic grade is variable. In contrast, ^{40}Ar/^{39}Ar muscovite data across the same region show a systematic decrease in age, from ~15 Ma in Nepal to ~7 Ma in Arunachal. This trend suggests that high-grade rocks at the uppermost structural levels of the GHS in the eastern Himalaya have cooled later than similar rocks in the central Himalaya.

Supplementary data to this article can be found online at http://dx.doi.org/10.1016/j.lithos.2014.04.005.

References

Beaumont, C., Jamieson, R.A., Nguyen, M.H., Lee, B., 2001. Himalayan tectonics explained by extrusion of a low-viscosity crustal channel coupled to focused surface denudation. Nature (London) 414, 738–742.

Beaumont, C., Nguyen, M., Jamieson, R.A., Ellis, S., 2006. Crustal flow modes in large hot orogens. In: Law, R.D., Searle, M.P., Godin, L. (Eds.), Channel Flows, Ductile Extrusion and Exhumation in Continental Collision Zones. Geological Society London Special Publications, 268, pp. 91–145.

Bhattacharya, A., Mohanty, L., Maji, A., Sen, S.K., Raith, M., 1992. Non-ideal mixing in the phlogopite–annite binary: constraints from experimental data on Mg–Fe partitioning and a reformulation of the biotite–garnet geothermometer. Contributions to Mineralogy and Petrology 111, 87–93. http://dx.doi.org/10.1007/BF00296580.

Bikramaditya, S.R.K., Singh, A.K., 2014. Microstructural and geochemical studies of Higher Himalayan Leucogranite: implications for geodynamic evolution of Tertiary Leucogranite in the Eastern Himalaya. Geological Journal 49, 28–51. http://dx.doi.org/10.1002/gj.2480.

Burchfiel, B.C., Chen, Z., Hodges, K.V., Liu, Y., Royden, L.H., Deng, C., Xu, J., 1992. The South Tibetan detachment system, Himalaya orogen: extension contemporaneous with and

parallel to shortening in a collisional mountain belt. Geological Society of America Special Paper 269 (41 p.).

Carosi, R., Lombardo, B., Molli, G., Musumeci, G., Pertusati, P.C., 1998. The south Tibetan detachment system in the Rongbuk valley, Everest region. Deformation features and geological implications. Journal of Asian Earth Sciences 16, 299–311. http://dx.doi.org/10.1016/S0743-9547(98)00014-2.

Chakungal, J., Dostal, J., Grujic, D., Duchêne, S., Ghalley, K.S., 2010. Provenance of the Greater Himalayan sequence: Evidence from mafic granulites and amphibolites in NW Bhutan. Tectonophysics 480, 198–212. http://dx.doi.org/10.1016/j.tecto.2009.10.014.

Copeland, P., Harrison, T.M., Hodges, K.V., Maruéjol, P., Le Fort, P., Pecher, A., 1991. An Early Pliocene thermal disturbance of the main central thrust, central Nepal: implications for Himalayan tectonics. Journal of Geophysical Research-Solid Earth and Planets 96, 8475–8500. http://dx.doi.org/10.1029/91JB00178.

Corrie, S.L., Kohn, M.J., 2011. Metamorphic history of the central Himalaya, Annapurna region, Nepal, and implications for tectonic models. Geological Society of America Bulletin 123, 1863–1879. http://dx.doi.org/10.1130/B30376.1.

Daniel, C.G., Hollister, L.S., Parrish, R.R., Grujic, D., 2003. Exhumation of the Main Central Thrust from lower crustal depths, eastern Bhutan Himalaya. Journal of Metamorphic Geology 21, 317–334.

Dodson, M.H., 1973. Closure temperature in cooling geochronological and petrological systems. Contributions to Mineralogy and Petrology 40, 259–274.

Gansser, A., 1974. Himalaya. Mesozoic Cenozoic Orogenic Belts: Data for Orogenic Studies. Geological Society of London, Special Publication, London, 4, pp. 267–278.

Gansser, A., 1983. Geology of the Bhutan Himalaya. Birkaeuser Verlag, Basel.

Greenwood, L.V., 2013, Orogenesis in the Eastern Himalayas: A study of structure, geochronology and metamorphism in Bhutan, unpubl. PhD thesis, the Open University, UK.

Grujic, D., Casey, M., Davidson, C., Hollister, L.S., Kündig, R., Pavlis, T., Schmid, S., 1996. Ductile extrusion of the Higher Himalayan Crystalline in Bhutan: evidence from quartz microfabrics. Tectonophysics 260, 21–43.

Grujic, D., Warren, C.J., Wooden, J.L., 2011. Rapid synconvergent exhumation of Miocene-aged lower orogenic crust in the eastern Himalaya. Lithosphere 3, 346–366. http://dx.doi.org/10.1130/L154.1.

Harrison, T.M., Duncan, I., McDougall, I., 1985. Diffusion of ^{40}Ar in biotite: temperature, pressure and compositional effects. Geochimica et Cosmochimica Acta 49, 2461–2468. http://dx.doi.org/10.1016/0016-7037(85)90246-7.

Harrison, T.M., Célérier, J., Aikman, A.B., Hermann, J., Heizler, M.T., 2009. Diffusion of ^{40}Ar in muscovite. Geochimica et Cosmochimica Acta 73, 1039–1051. http://dx.doi.org/10.1016/j.gca.2008.09.038.

Hauck, M.L., Nelson, K.D., Brown, L.D., Zhao, W., Ross, A.R., 1998. Crustal structure of the Himalayan orogen at ~90° east longitude from Project INDEPTH deep reflection profiles. Tectonics 17, 481–500. http://dx.doi.org/10.1029/98TC01314.

Henry, D.J., Guidotti, C.V., Thomson, J.A., 2005. The Ti-saturation surface for low-to-medium pressure metapelitic biotites: implications for geothermometry and Ti-substitution mechanisms. American Mineralogist 90, 316–328. http://dx.doi.org/10.2138/am.2005.1498.

Hiess, J., Condon, D.J., McLean, N., Noble, S., 2012. ^{238}U/^{235}U systematics in terrestrial uranium-bearing minerals. 335, 610–614. http://dx.doi.org/10.1126/science.1215507.

Hodges, K.V., 2000. Tectonics of the Himalaya and southern Tibet from two perspectives. GSA Bulletin 112, 324–350. http://dx.doi.org/10.1130/0016-7606(2000)112<324:TOTHAS>2.0.CO;2.

Holdaway, M.J., 2000. Application of new experimental and garnet Margules data to the garnet–biotite geothermometer. American Mineralogist 85, 881–892.

Holdaway, M.J., Lee, S.M., 1977. Fe–Mg cordierite stability in high-grade pelitic rocks based on experimental, theoretical and natural observations. Contributions to Mineralogy and Petrology 63, 175–198.

Holland, T.J.B., Powell, R., 1998. An internally consistent thermodynamic data set for phases of petrological interest. Journal of Metamorphic Geology 16, 309–343. http://dx.doi.org/10.1111/j.1525-1314.1998.00140.x.

Horstwood, M.S.A., 2008. Data reduction strategies, uncertainty assessment and resolution of LA-(MC)-ICP-MD isotope data. In: Sylvester, P. (Ed.), Laser Ablation ICP-MS in the Earth Sciences: Current Practices and Outstanding Issues. Mineralogical Association of Canada (Short Courses), pp. 283–303.

Imayama, T., Takeshita, T., Yi, K., Cho, D., Kitajima, K., Tsutsumi, Y., Kayama, M., Nishido, H., Okumura, T., Yagi, K., Itaya, T., Sano, Y., 2012. Two-stage partial melting and contrasting cooling history within the Higher Himalayan Crystalline Sequence in the far-eastern Nepal Himalaya. Lithos 134–135, 1–22. http://dx.doi.org/10.1016/j.lithos.2011.12.004.

Jamieson, R.A., Beaumont, C., 2013. On the origin of orogens. Geological Society of America Bulletin 125, 1671–1702. http://dx.doi.org/10.1130/B30855.1.

Jamieson, R.A., Beaumont, C., Nguyen, M.H., Grujic, D., 2006. Provenance of the Greater Himalayan Sequence and associated rocks; predictions of channel flow models; channel flow, ductile extrusion and exhumation in continental collision zones. Geological Society of London, Special Publication 268, 165–182.

Kellett, D.A., Grujic, D., Erdmann, S., 2009. Miocene structural reorganization of the South Tibetan detachment, eastern Himalaya: implications for continental collision. Lithosphere 1, 259–281. http://dx.doi.org/10.1130/L56.1.

Kellett, D.A., Grujic, D., Warren, C.J., Cottle, J., Jamieson, R.A., Tenzin, T., 2010. Metamorphic history of a syn-convergent orogen-parallel detachment: the South Tibetan detachment system, eastern Himalaya. Journal of Metamorphic Geology 28, 785–808. http://dx.doi.org/10.1111/j.1525-1314.2010.00893.x.

Kellett, D.A., Grujic, D., Coutand, I., Cottle, J., Mukul, M., 2013. The South Tibetan detachment system facilitates ultra rapid cooling of granulite-facies rocks in Sikkim Himalaya. Tectonics 32, 252–270. http://dx.doi.org/10.1002/tect.20014.

Ludwig, K.K., 2001. Isoplot/Ex version 2.49. A geochronological toolkit for Microsoft Excel. Berkeley Geochronology Centre, Special Publication.

Maluski, H., Matte, P., Brunel, M., Xiao, X., 1988. ^{40}Ar/^{39}Ar dating of metamorphic and plutonic events in the North and High Himalaya Belts (Southern Tibet, China). Tectonics 7, 299–326.

McDougall, I, Harrison, T.M., 1999. Geochronology and Thermochronology by the ^{40}Ar/^{39}Ar Method. Oxford University Press p. 269.

Mottram, C.M., Parrish, R.R., Warren, C.J., Regis, D., Roberts, N.M.W., Argles, T.W., Harris, N.B.W., 2014w. Petrochronology of an inverted metamorphic sequence. Earth and Planetary Science Letters. (in review).

Palin, R.M., Searle, M.P., Waters, D.J., Parrish, R.R., Roberts, N.M.W., Horstwood, M.S.A., Yeh, M.-W., Chung, S.-L., Anh, T.T., 2013. A geochronological and petrological study of anatectic paragneiss and associated granite dykes from the Day Nui Con Voi metamorphic core complex, North Vietnam: constraints on the timing of metamorphism within the Red River shear zone. Journal of Metamorphic Geology 31, 359–387. http://dx.doi.org/10.1111/jmg.12025.

Regis, D., Warren, C.J., Young, D., Roberts, N.M.W., 2014. Tectono-metamorphic evolution of the Jhomolari massif: variations in timing of syn-collisional metamorphism across western Bhutan. Lithos 190–191, 449–466. http://dx.doi.org/10.1016/j.lithos.2014.01.001.

Renne, P.R., Swisher, C.C., Deino, A.L., Karner, D.B., Owens, T.L., DePaolo, D.J., 1998. Intercalibration of standards, absolute ages and uncertainties in ^{40}Ar/^{39}Ar dating. Chemical Geology 145, 117–152. http://dx.doi.org/10.1016/S0009-2541(97)00159-9.

Rowley, D.B., 1996. Age of initiation of collision between India and Asia: a review of stratigraphic data. Earth and Planetary Science Letters 145, 1–13. http://dx.doi.org/10.1016/S0012-821X(96)00201-4.

Rowley, D.B., 1998. Minimum age of initiation of collision between India and Asia North of Everest based on the subsidence history of the Zhepure mountain section. The Journal of Geology 106, 220–235.

Rubatto, D., Chakraborty, S., Dasgupta, S., 2013. Timescales of crustal melting in the Higher Himalayan Crystallines (Sikkim, Eastern Himalaya) inferred from trace element-constrained monazite and zircon chronology. Contributions to Mineralogy and Petrology 165, 349–372. http://dx.doi.org/10.1007/s00410-012-0812-y.

Sherlock, S.C., Lucks, T., Kelley, S.P., Barnicoat, A., 2005. A high resolution record of multiple diagenetic events: ultraviolet laser microprobe Ar/Ar analysis of zoned K-feldspar overgrowths. Earth and Planetary Science Letters 238, 329–341. http://dx.doi.org/10.1016/j.epsl.2005.07.018.

Sherlock, S.C., Jones, K.A., Park, R.G., 2008. Grenville-age pseudotachylite in the Lewisian: laserprobe ^{40}Ar/^{39}Ar ages from the Gairloch region of Scotland (UK). Journal of the Geological Society (London) 165, 73–83. http://dx.doi.org/10.1144/0016-76492006-134.

Simpson, R.L., Parrish, R.R., Searle, M.P., Waters, D.J., 2000. Two episodes of monazite crystallization during metamorphism and crustal melting in the Everest region of the Nepalese Himalaya. Geology 28, 403–406. http://dx.doi.org/10.1130/0091-7613(2000)28<403:TEOMCD>2.0.CO;2.

Stacey, J.S., Kramers, J.D., 1975. Approximation of terrestrial lead isotope evolution by a two-stage model. Earth and Planetary Science Letters 26, 207–221. http://dx.doi.org/10.1016/0012-821X(75)90088-6.

Steiger, R.H., Jäger, E., 1977. Subcommission on geochronology: convention on the use of the decay constants in geo- and cosmochronology. Earth and Planetary Science Letters 36, 359–362.

Stüwe, K., Foster, D., 2001. ^{40}Ar/^{39}Ar, pressure, temperature and fission track constraints on the age and nature of metamorphism around the main central thrust in the eastern Bhutan Himalaya. Journal of Asian Earth Sciences 19, 85–95.

Tobgay, T., Long, S., McQuarrie, N., Ducea, M.N., Gehrels, G., 2010. Using isotopic and chronologic data to fingerprint strata: challenges and benefits of variable sources to tectonic interpretations, the Paro Formation, Bhutan Himalaya. Tectonics 29, TC6023. http://dx.doi.org/10.1029/2009TC002637.

Tobgay, T., McQuarrie, N., Long, S., Kohn, M.J., Corrie, S.L., 2012. The age and rate of displacement along the Main Central Thrust in the western Bhutan Himalaya. Earth and Planetary Science Letters 319–320, 146–158. http://dx.doi.org/10.1016/j.epsl.2011.12.005 (15 February).

Villa, 1998. Isotopic closure. Terra Nova 10, 42–47. http://dx.doi.org/10.1046/j.1365-3121.1998.00156.x.

Viskupic, K., Hodges, K., Bowring, S., 2005. Timescales of melt generation and the thermal evolution of the Himalayan metamorphic core, Everest region, eastern Nepal. Contributions to Mineralogy and Petrology 149, 1–21. http://dx.doi.org/10.1007/s00410-004-0628-5.

Warren, C.J., Beaumont, C., Jamieson, R.A., 2008. Modelling tectonic styles and ultra-high pressure (UHP) rock exhumation during the transition from oceanic subduction to continental collision. Earth and Planetary Science Letters 267, 129–145. http://dx.doi.org/10.1016/j.epsl.2007.11.025.

Warren, C.J., Grujic, D., Kellett, D.A., Cottle, J., Jamieson, R.A., Ghalley, K.S., 2011a. Probing the depths of the India–Asia collision: U–Th–Pb monazite chronology of granulites from NW Bhutan. Tectonics 30, TC2004. http://dx.doi.org/10.1029/2010TC002738.

Warren, C.J., Sherlock, S.C., Kelley, S.P., 2011b. Interpreting high-pressure phengite ^{40}Ar/^{39}Ar laserprobe ages: an example from Saih Hatat, NE Oman. Contributions to Mineralogy and Petrology 161, 991–1009. http://dx.doi.org/10.1007/s00410-010-0576-1.

Warren, C.J., Grujic, D., Cottle, J.M., Rogers, N.W., 2011c. Constraining cooling histories: rutile and titanite chronology and diffusion modelling in NW Bhutan. Journal of Metamorphic Geology 30, 113–130. http://dx.doi.org/10.1111/j.1525-1314.2011.00958.x.

Warren, C.J., Smye, A.J., Kelley, S.P., Sherlock, S.C., 2012a. Using white mica ^{40}Ar/^{39}Ar data as a tracer for fluid flow and permeability under high-P conditions: Tauern Window,

Eastern Alps. Journal of Metamorphic Geology 30, 63–80. http://dx.doi.org/10.1111/j. 1525-1314.2011.00956.x.

Warren, C.J., Hanke, F., Kelley, S.P., 2012b. When can muscovite ^{40}Ar/^{39}Ar dating constrain the timing of metamorphic exhumation? Chemical Geology 291, 79–86. http://dx.doi. org/10.1016/j.chemgeo.2011.09.017.

Warren, C.J., Kelley, S.P., Sherlock, S.C., McDonald, C.S., 2012c. Metamorphic rocks seek meaningful cooling rate: interpreting ^{40}Ar/^{39}Ar ages in an exhumed ultra-high pressure terrane. Lithos 155, 30–48. http://dx.doi.org/10.1016/j.lithos. 2012.08.011.

Wheeler, J., 1996. Diffarg: a program for simulating argon diffusion profiles in minerals. Computers & Geosciences 22, 919–929. http://dx.doi.org/10.1016/S0098-3004(96) 00061-1.

Whitney, D.L., Evans, B.W., 2010. Abbreviations for names of rock-forming minerals. American Mineralogist 95, 185–187. http://dx.doi.org/10.2138/am.2010.3371.

Wu, C., Wang, X., Yang, C., Geng, Y., Liu, F., 2002. Empirical garnet–muscovite geothermometry in metapelites. Lithos 62, 1–13. http://dx.doi.org/10.1016/S0024-4937(02)00096-8.

Wu, C., Zhang, J., Ren, L., 2004. Empirical garnet–muscovite–plagioclase–quartz geobarometry in medium- to high-grade metapelites. Lithos 78, 319–332. http://dx. doi.org/10.1016/j. lithos.2004.06.008.

Yin, A., Dubey, C.S., Kelty, T.K., Gehrels, G.E., Chou, C.Y., Grove, M., Lovera, O., 2006. Structural evolution of the Arunachal Himalaya and implications for asymmetric development of the Himalayan orogen. Current Science 90, 195–206.

Yin, A., Dubey, C.S., Kelty, T.K., Webb, A.A.G., Harrison, T.M., Chou, C.Y., Célérier, J., 2010. Geologic correlation of the Himalayan orogen and Indian craton: part 2. Structural geology, geochronology, and tectonic evolution of the Eastern Himalaya. Geological Society of America Bulletin 122, 360–395. http://dx.doi.org/10.1130/B26461.1.

Zhu, B., Kidd, W., Rowley, D., Currie, B., Shafique, N., 2005. Age of initiation of the India–Asia collision in the East-Central Himalaya. The Journal of Geology 113, 265–285.